Detecting trend and seasonal changes in bathymetry derived from HICO imagery: a case study of Shark Bay, Western Australia.

Rodrigo A. Garcia, [a, *] Peter R.C.S. Fearns, [a] and Lachlan I.W. McKinna.[a,b]

[a]Remote Sensing and Satellite Research Group, Department of Imaging and Applied Physics, Curtin University, GPO Box U1987, Perth, Western Australia, 6845.

[b]NASA Postdoctoral Program Fellow, Ocean Ecology Laboratory, Code 616, NASA Goddard Space Flight Center, Greenbelt, MD, 20771, USA.

Abstract

The Hyperspectral Imager for the Coastal Ocean (HICO) aboard the International Space Station has offered for the first time a dedicated space-borne hyperspectral sensor specifically designed for remote sensing of the coastal environment. However, several processing steps are required to convert calibrated top-of-atmosphere radiances to the desired geophysical parameter(s). These steps add various amounts of uncertainty that can cumulatively render the geophysical parameter imprecise and potentially unusable if the objective is to analyze trends and/or seasonal variability. This research presented here has focused on: (1) atmospheric correction of HICO imagery; (2) retrieval of bathymetry using an improved implementation of a shallow water inversion algorithm; (3) propagation of uncertainty due to environmental noise through the bathymetry retrieval process; (4) issues relating to consistent geo-location of HICO imagery necessary for time series analysis, and; (5) tide height corrections of the retrieved bathymetric dataset. The underlying question of

* Corresponding author. Tel.: +61 8 9266 1257
Email address: rodrigo.garcia@postgrad.curtin.edu.au

whether a temporal change in depth is detectable above uncertainty is also addressed. To this end, nine HICO images spanning November 2011 to August 2012, over the Shark Bay World Heritage Area, Western Australia, were examined. The results presented indicate that precision of the bathymetric retrievals are dependent on the shallow water inversion algorithm used. Within this study, an average of 70% of pixels for the entire HICO-derived bathymetry dataset achieved a relative uncertainty of less than ±20%. A per-pixel *t*-test analysis between derived bathymetry images at successive timestamps revealed observable changes in depth to as low as 0.4 m. However, the present geolocation accuracy of HICO is relatively poor and needs further improvements before extensive time series analysis can be performed.

1.0 Introduction

Detecting change in the near-shore coastal marine environment is necessary for understanding mechanisms that drive change in these dynamic systems. One important challenge for coastal marine managers is detecting change in bathymetry over large areas in a timely manner. With such information, informed decisions can be made for efficient and effective management of these fragile ecosystems (Fabbri, 1998; Galparsoro et al., 2010). The bathymetry of the near-shore could change seasonally or in response to acute disturbances, such as storms and extreme weather events (Morton, 2002; Morton and Sallenger, 2003), or human induced disturbances such as dredging (Cooper et al., 2007). These changes can have flow-on impacts to the marine flora and fauna that the marine resource managers are tasked to protect. As such, accurate bathymetric monitoring techniques that are time and cost effective are required to assess any residual geological and ecological impacts.

Accurate bathymetry maps can be achieved using active remote sensing such as an airborne LiDAR system (Irish and Lillycrop, 1999; Guenther et al., 2000). However, frequent long-term monitoring of large coastal areas can be costly even with airborne systems. Satellite-based passive remote sensing offers an even more cost effective means of obtaining bathymetry maps as it can repeatedly sample large areas (hundreds to thousands of square kilometers) frequently (Green et al., 1996). The temporal resolution and large spatial coverage makes satellite remote sensing ideal for monitoring changes in bathymetry over large areas.

One of the first quantitative methods of measuring bathymetry from multispectral imagery was proposed by Polcyn et al. (1970). This method manipulates the ratio of two spectral indices to generate a semi-empirical relationship for depth. This algorithm can remove the influence of varying water clarity and bottom reflectance only in very specific conditions (see Polcyn et al., 1970) that are rarely encountered in the coastal ocean.

Lyzenga (1978) proposed a linearized multiband bathymetry algorithm that corrects for bottom type variation. This algorithm however requires a depth calibration from *in situ* depth data and, as such, the approach is scene-specific (Paredes and Spero, 1983; Lyzenga, 1985; Clark et al., 1987) though has been shown to give improved results over the band ratio algorithm of Polcyn et al. (1970) (Clark et al., 1987). Practical complications arise when a scene has varying water clarity and undefined depths when the water leaving reflectance of a shallow area is less than that over deep water (Philpot, 1989). Other algorithms that use *in situ* depth data for tuning empirical coefficients include Dierssen et al. (2003) and Stumpf et al. (2003), both of which use spectral band ratios.

Although the algorithms proposed by Lyzenga (1978), Dierssen et al. (2003) and Stumpf et al. (2003) can be accurate with imagery that fit their empirical constraints, they still require *in situ* depth data which often is not available, historically or con-currently. Thus for

the purposes of transferability between sensors and scenes, it is crucial to have bathymetric algorithms that circumvent the need for *in situ* data.

Semi-analytical, physics-based shallow water inversion algorithms (HOPE in Lee et al., 1998; 1999; BRUCE in Klonowski et al., 2007; SAMBUCA in Wettle and Brando, 2006 and Brando et al., 2009) and Look-up-table (LUT) techniques (CRISTAL in Mobley et al., 2005; ALLUT in Hedley et al., 2009) designed for hyperspectral sensors, appear to be more suitable for retrieving bathymetry, water column inherent optical properties (IOPs) and for rudimentary benthic classification (Dekker and Phinn et al. 2011). An advantage of semi-analytical algorithms is their non-reliance on possibly erroneous assumptions of uniform water IOPs or bottom reflectance, or crude corrections (e.g. the deep water radiance correction). Instead, semi-analytical algorithms are derived from radiative transfer theory making them more analytically exact with lower sources of model error. Consequently, they have been used to retrieve bathymetry with relatively high accuracy from airborne hyperspectral imagery captured over optically complex coastal marine environments (Mobley et al., 2005; Klonowski et al., 2007; Brando et al., 2009; Hedley et al., 2009; Dekker and Phinn et al., 2011).

Shallow water semi-analytical inversion algorithms rely on spectral matching and/or optimization routines which require image data with enough spectral bands in the visible domain (typically: 400 – 800 nm) to resolve subtle optical signatures. Hyperspectral image data with a modest signal-to-noise ratio (SNR) can achieve this (Philpot et al., 2003). Moreover, the spectral information provided by hyperspectral imagery minimizes non-uniqueness issues, resulting in lower confidence interval limits of the retrieved parameters (Defoin-Platel and Chami, 2007; Mobley et al., 2005). The lack of accessible hyperspectral satellite imagery has limited the applicability of the physics-based semi-analytical algorithms to airborne hyperspectral imagery. However, there have been a few examples in the literature,

such as Lee et al. (2007), who used HOPE to retrieve the spatial distribution of water absorption, depth and bottom reflectance from Hyperion imagery of Looe Key, Florida, USA.

Although the Hyperion sensor has over 200 spectral bands between 430-2400 nm, it was designed primarily for land-use applications and as such has a relatively low SNR that ranges from 50-150 (Ungar, 2003). Over dark targets, such as water, a low SNR effectively creates a 'noisier' signal and subtle changes in the reflectance spectrum may not be differentiated above the noise inherent to the sensor (Hu et al., 2012). This confounds the remote sensing signal leading to non-uniqueness and hence higher uncertainty of the retrieved parameter(s). However, as stated by Lee et al. (2007), many shallow coastal areas are subject to high water turbidity resulting from suspended sediment run-off or where the water-leaving radiance signal has significant contribution from a bright bottom substrate, thus in such cases, Hyperion may have a high enough SNR to afford results with higher confidence. These represent a limited range of coastal environmental conditions suitable for Hyperion applications, as these waters may also be subject to highly absorbing waters (due to phytoplankton and/or colored dissolved organic matter), dark bottom substrates (such as seagrass and algae), and large bathymetric ranges that requires higher SNR for more accurate assessments.

The Hyperspectral Imager for the Coastal Ocean (HICO) is the first prototype, low cost sensor onboard the International Space Station designed with the necessary specifications for remote sensing of a diverse range of coastal marine environments (Lucke et al., 2011). HICO has a spatial resolution of 96 × 96 m at nadir with 87 contiguous spectral bands between 400-900 nm. HICO's SNR varies spectrally but is generally greater than 200 between 400 and 600 nm, and ranges from 100-200 between 600 and 700 nm (Lucke et al., 2011). These sensor attributes make HICO suitable for analyzing the spectral and spatial complexity encountered in many coastal marine environments throughout the globe.

To date, there has been limited work reported on the routine monitoring of bathymetry using standardized processing of satellite hyperspectral imagery. In this paper, the semi-analytical Bottom Reflectance Un-mixing Computation of the Environment inversion algorithm (BRUCE: Klonowski et al., 2007) is used to retrieve bathymetry from multi-temporal HICO imagery of the Shark Bay World Heritage Area, Western Australia. We focus on the Faure Sill, a shallow region within Shark Bay noted for its unique seascape and ecological features. The aims of this research were: (1) to test whether a change in bathymetry is measurable above statistical uncertainty through time; (2) examine the robustness of the Tafkaa (Gao et al. 2000) atmospheric model when applied to HICO imagery whose spectral range does not extend beyond 900 nm; (3) to determine the precision of a HICO-derived bathymetric dataset using an improved implementation of the BRUCE model, specifically redesigned to allow uncertainty propagation; (4) compare tide correction techniques and; (5) to study the geolocation accuracy of HICO imagery and its implication to routine monitoring.

2.0 Methodology

2.1 Study area and HICO imagery

Shark Bay is a World Heritage Area located in the northwest of Western Australia (Figure 1), covering an area of ~14 000 km^2. This shallow coastal bay has two major sub-embayments orientated in a NW-SE direction; Freycinet Reach, located to the west of the Peron peninsula, and Hopeless Reach on the east. In this case study we limit our analysis to Hopeless Reach with focus on the Faure Sill; a shallow (1-2 m in depth) region ~30 km long and ~15 km wide, containing several narrow water channels (5-6 m in depth) extending into Hamelin Pool and which run parallel to the tidal currents (Walker et al., 1988; Burling et al., 2003). Shark Bay's seascape, ecology and corresponding hydrodynamics are inter-related and

unique. Semi-enclosed by three islands, Shark Bay experiences limited oceanic exchange and mixing, and combined with low annual rainfall (low land runoff) results in calm waters (Department of Environment and Conservation, no date). These are favorable conditions for seagrasses which cover ~4200 km^2 of Shark Bay (Walker et al., 1988). These extensive seagrass meadows influence the sedimentation processes within Shark Bay and over time have created large sand banks (e.g. the Faure Sill) that restrict water movement into Hamelin Pool, a unique hypersaline region inhabited by stromatolites (Logan and Cebulski, 1970).

A total of nine HICO images, each with a central image coordinate of ~25.9 °S/113.9 °E, were captured over Shark Bay, Western Australia, from 19 November 2011 to 8 August 2012. Pseudo true color imagery of the HICO dataset are displayed in Figure 2. Two different swath orientations of HICO were observed: NW-SE and SW-NE, with the Faure Sill captured within successive swaths. Though each swath had the same coverage/footprint, they often appeared to have a slight translational drift (illustrated in Figure 1).

All HICO image data and geographic look-up-tables (GLTs) used in this study were accessed through the Oregon State University, College of Earth, Ocean, and Atmospheric Sciences, HICO web portal (hico.coas.oregonstate.edu). Note, the distributed HICO level-1B (L1B) calibrated radiance files had both spectral and radiometric vicarious calibrations (Gao et al., 2012) and, second order light effect corrections applied (Li et al., 2012).

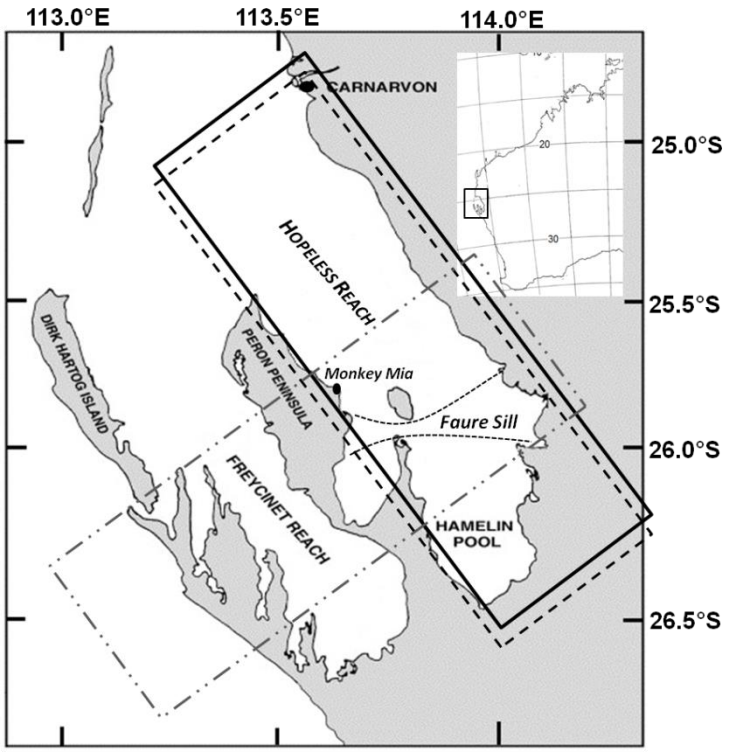

Figure 1: Shark Bay, Western Australia, with the Faure Sill located between the two curved black dotted lines. The solid black and dot-dot-dashed grey rectangles show the different approximate orientations of the HICO swaths. The dashed black rectangle illustrates the translational drift in the HICO swath position.

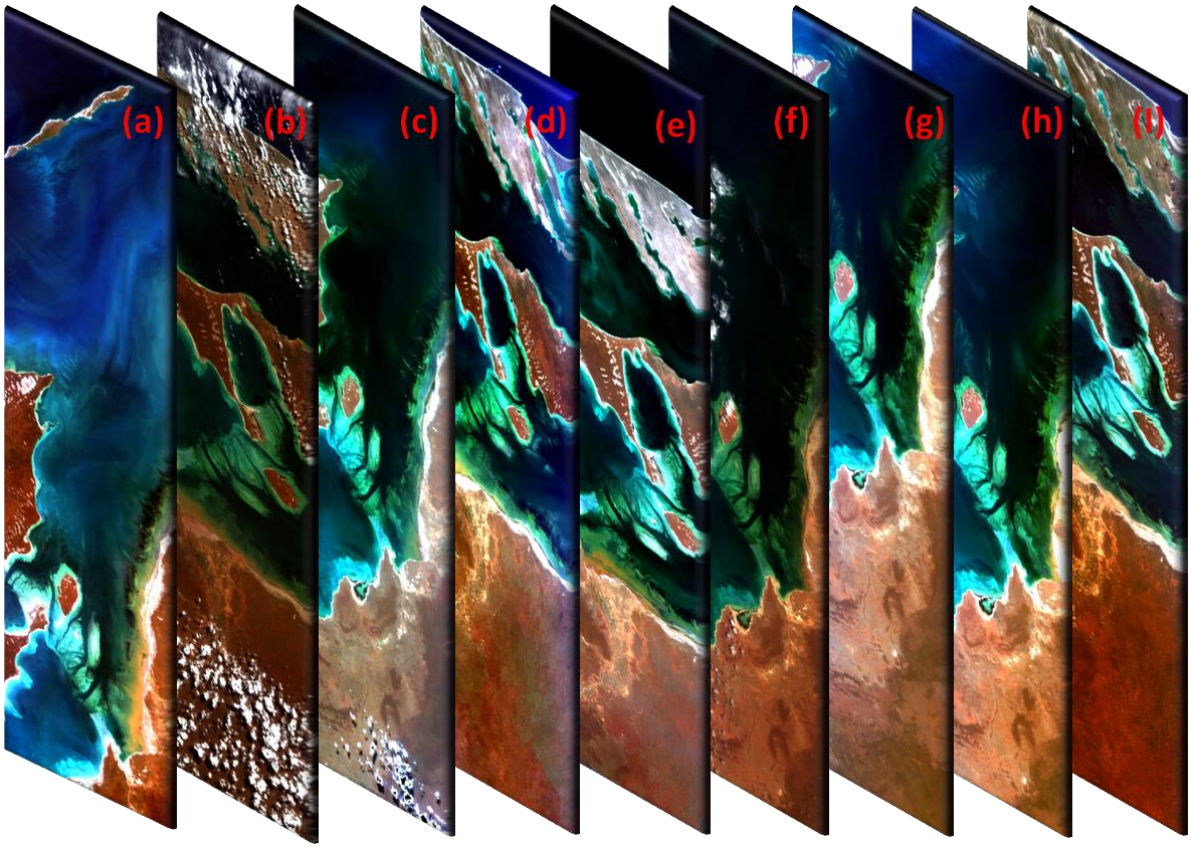

Figure 2: pseudo true color composites of the HICO remote sensing reflectance imagery over Shark Bay, WA, on: (a) 19-Nov-2011; (b) 14-Dec-11; (c) 21-Jan-2012; (d) 07-Feb-12; (e) 27-Feb-12; (f) 02-Apr-12; (g) 01-Jun-12; (h) 04-Jun-12, and; (i) 08-Aug-12. The apparent illumination variation between these images is due to the different scaling used to generate the pseudo true color composites.

2.2 Atmospheric Correction

The Second Simulation of the Satellite Signal in the Solar Spectrum (6S) implementation of Tafkaa algorithm (Gao et al., 2000) was used to atmospherically correct the L1B, calibrated top-of-atmosphere radiance imagery. The standard Tafkaa 6S algorithm uses several bands greater than 900 nm to estimate key atmospheric parameters - namely, the aerosol model, the aerosol optical thickness, AOT, at 550 nm, the vertical column water vapor, ozone concentration and the atmospheric and aerosol models in a per-pixel basis (Gao et al., 2000). However, HICO lacks any SWIR and IR (> 900 nm) bands and thus limits the application of Tafkaa 6S. Previous research has highlighted the importance of selecting

appropriate AOT values for Tafkaa when atmospherically correcting HICO scenes (Paterson and Lamela, 2011). Therefore, within this study, coincident MODerate resolution Imaging Spectroradiometer (MODIS) Level-2 data of Shark Bay were used to estimate the AOT at 550 nm, vertical column water vapor, CLMVAP, and ozone concentration which were then used to parameterize the Tafkaa 6S algorithm. The MODIS imagery of Shark Bay, were downloaded from the Ocean Biology Processing Group data browse website (http://oceancolor.gsfc.nasa.gov/cgi/browse.pl?sen=am) and processed from raw radiance counts (level 0) to calibrated Top-Of-Atmosphere radiance (level-1B). The standard MODIS ocean color atmospheric correction algorithm (Ahmad et al., 2010; Bailey et al., 2010) implemented in SeaDAS 6.4 was then used to obtain the three atmospheric properties.

Simplified at-nadir viewing geometry was assumed and the Tafkaa 6S aerosol and atmospheric model were fixed to "maritime" and "mid-latitude summer" respectively for all HICO scenes as these were deemed the most appropriate for Shark Bay. Hence Tafkaa 6S was not used to solve for any atmospheric properties using HICO's NIR bands; rather it removed the atmospheric radiance signal based on predefined inputs. Note: (1) MODIS data were not used to select these Tafkaa 6S models; (2) the vertical pressure, temperature and relative humidity profiles are described in the atmospheric model; (3) given the atmospheric model and the atmospheric water vapor, Tafkaa 6S then determines the vertical structure of the water vapor (Montes et al., 2004), and; (4) the aerosols in Tafkaa 6S all assume 70% relative humidity (Montes et al., 2004).

Table 1: MODIS-derived vertical column of water vapor (CLMVAP), aerosol optical thickness at 550 nm (AOT) and ozone concentration, with the solar-viewing geometries for each HICO overpass of Shark Bay, WA. The time presented is in Australian Western Standard Time (WST; UTC +8 hours). Here θ_s, θ_v and φ are the viewing solar, viewing zenith and relative azimuth angles respectively.

HICO overpass	MODIS overpass	CLMVAP (cm)	AOT (550 nm)	Ozone (atm-cm)	θ_s (°)	θ_v (°)	φ (°)
19-Nov-11, 1632 hrs	19-Nov, 1435 hrs	1.8	0.08	0.28	60.02	21.4	-214.1
14-Dec-11, 1539 hrs	14-Dec, 1425 hrs	2.0	0.1	0.27	45.25	6.3	-128.6
21-Jan-12, 1538 hrs	21-Jan, 1350 hrs	2.7	0.15	0.26	42.45	23.2	-41.98
07-Feb-12, 1722 hrs	07-Feb, 1435 hrs	3.0	0.15	0.25	66.50	36.6	-128.96
27-Feb-12, 0940 hrs	27-Feb, 1410 hrs	3.0	0.35	0.25	45.47	13.4	58.35
02-Apr-12, 1035 hrs	02-Apr, 1440 hrs	2.3	0.055	0.26	41.06	20.8	1.12
01-Jun-12, 1038 hrs	01-Jun*, 0005 hrs	1.7	0.035	0.26	53.99	16.1	16.93
04-Jun-12, 0932 hrs	04-Jun, 1355 hrs	1.0	0.035	0.26	63.31	4.09	2.25
08-Aug-12, 1625 hrs	08-Aug, 1440 hrs	1.45	0.045	0.27	71.00	16.7	-165.56

* MODIS Terra

The lack of concurrent *in situ* above-water radiometry/photometry and AERONET data prevented a quantitative measure of the accuracy of the atmospheric correction. However, a cursory evaluation of the atmospheric correction was performed by examining the reflectance

spectra for two locations representing: (i) bright shallow water (25.907 °S/113.934 °E), and (ii) quasi-deep water (25.718 °S/113.978 °E), through time. It should be noted that atmospheric correction removes approximately 90% of the signal that any satellite sensor records. Thus under- or over-corrections and spectral artifacts introduced to R_{rs} can be delineated from changes in the optical properties of the water column at these positions through time.

2.3 Retrieval of bathymetry using the BRUCE model

According to Lee et al. (1998, 1999), the hyperspectral sub-surface remote sensing reflectance signal, $r_{rs}(\lambda)$, of a shallow water pixel can be modeled as a function of the total in-water spectral absorption and backscattering coefficients, $a(\lambda)$ and $b_b(\lambda)$, the spectral benthic albedo, $\rho(\lambda)$, the geometric depth (which we are attempting to solve for), H, the sub-surface solar zenith angle, θ_w, and the sub-surface viewing angle from nadir, θ_v.

$$r_{rs}(\lambda) = f(a(\lambda), b_b(\lambda), H, \rho(\lambda), \theta_v, \theta_w) \quad (1)$$

The view and solar geometries can be considered as fixed, or known. The total absorption coefficient is a function of the absorption of pure water, phytoplankton and color dissolved organic and detrital matter (CDM), whilst the backscattering coefficient is function of the backscattering of pure water and suspended particulates, as given by,

$$a(\lambda) = a_w(\lambda) + P\, a_\phi(\lambda) + G\, e^{-0.015(\lambda - 440)}$$

$$b_b(\lambda) = b_{bw}(\lambda) + X\left(\frac{550}{\lambda}\right)^{1.0} \quad (2)$$

$$\rho(\lambda) = \sum_{i=1}^{n=3} B_i \rho_i(\lambda)$$

where a_w and b_{bw} are the spectral absorption and backscattering coefficients of pure water, respectively. a_ϕ is the spectral absorption coefficient of phytoplankton normalized at 440 nm; B_i is the bottom albedo coefficient at 550 nm and ρ_i is spectral irradiance reflectance

normalized at 550 nm of benthic class *i*, respectively. The scalars *P* and *G* are the magnitudes of the absorption coefficients of phytoplankton and CDM respectively, whilst *X* is the magnitude of the particulate backscattering coefficient. Thus, the shallow water forward model can be expressed as:

$$r_{rs}(\lambda) = f(P, G, X, H, B, \theta_v, \theta_w) \quad (3)$$

Though the spectral shapes and slopes of the optically active in-water constituents and benthic end-members were predefined and fixed, their magnitudes (*P*, *G*, *X*, B_i), including the depth, are solved using the Levenberg-Marquardt algorithm. This non-linear least-squares optimization compares sensor-derived with modeled r_{rs} values, and once the solution converges, the best fit values of *P*, *G*, *X*, B_i and *H* are deemed to have been solved. Further comprehensive detail of physics-based semi-analytical shallow water inversion algorithms can be found in Dekker and Phinn et al. (2011) and references therein.

Within this study we have used the BRUCE model, developed by Klonowski et al. (2007). This semi-analytical shallow water model is a variant of the Hyperspectral Optimization Process Exemplar model, HOPE, proposed by Lee et al. (1998; 1999). The difference arises in the parameterization of the benthic albedo, $\rho(\lambda)$. Unlike HOPE, which considers the net benthic albedo is due to only a single benthic substrate, BRUCE assumes the net benthic albedo to be a spectral mixture of three benthic end-members. In this research, we express the bottom albedo as a linear mix of two benthic classes, sand and mixed seagrass (50% *Posidonia australis* and 50% *Amphibolis antartica*). These two species of seagrass were previously recorded as the most dominant across Shark Bay (Walker et al., 1988). The irradiance reflectance spectra of sand, *P. australis* and *A. antartica* were measured using a handheld hyperspectral radiometer during a field campaign to Shark Bay.

Tafkaa 6S outputs R_{rs} that are not corrected for specular reflection of direct solar and sky radiance from the ocean surface (Montes et al., 2004). Thus before implementing the

non-linear least squares optimization, the R_{rs} spectra were corrected for sunglint contamination using a correction scheme based on Lee et al. (1999) and Goodman et al. (2008),

$$R_{rs}(\lambda) = R_{rs}^{raw}(\lambda) - \gamma + \Delta$$
$$\Delta = 1.9 \times 10^{-5} + 0.1[R_{rs}^{raw}(640) - \gamma] \quad (4)$$
$$\gamma = \min\left(R_{rs}^{raw}(640) : R_{rs}^{raw}(750)\right)$$

where γ is the lowest R_{rs}^{raw} value between 640 and 750 nm. Note that γ was included to avoid negative reflectances if the R_{rs}^{raw} of a wavelength shorter than 750 nm was less than that at 750 nm. Whilst there are other sun-glint corrections in the literature (see Kay et al., 2009), Goodman et al. (2008), used a similar correction to equation 4 and obtained quite accurate depth retrievals for shallow waters of Kaneohe Bay, Hawaii. Sub-surface remote sensing reflectances were then computed using (Lee et al., 1999; IOCCG, 2006),

$$r_{rs}(\lambda) = \frac{R_{rs}}{(0.51 - 1.5R_{rs})} \quad (5)$$

A two-step inversion approach was used to retrieve depth that included: (1) a brief search of the parameter space for the optimal initial guess parameters used in the BRUCE model, and; (2) the uncertainty propagation scheme proposed by Hedley et al. (2010; 2012).

As stated by Hedley et al. (2010), the uncertainty procedure begins with computing the spectral covariance matrix from a homogeneous deep water region of the image. The Cholesky decomposition matrix, *L*, is then calculated from the covariance matrix. The procedure then iterates through the r_{rs} image where, for each pixel, the *L* matrix is used to compute 20 noise-perturbed r_{rs} spectra, $r_{rs} + \delta r_{rs}$. Each spectrally correlated noise term, δr_{rs}, is generated by product multiplication of the *L* matrix by an *n*-band vector, whose values are normally distributed random numbers ($\mu = 0$, $\sigma = 1$). The BRUCE model, through non-linear least squares optimization provided by the Levenberg-Marquardt (L-M) algorithm, then retrieves the values of *P*, *G*, *X*, *H*, B_{sand} and $B_{seagrass}$ for each noise-perturbed r_{rs} spectrum.

The mean and standard deviation are then computed for each parameter set, where the former is taken to be the actual retrieved parameter value and the latter its uncertainty.

In the standard implementation of BRUCE, the initial guess parameters used to initiate the L-M optimization routine are kept constant for all pixels in an image. However, analysis (results not presented here) has shown that different initial guess values lead to different local minima having different Euclidean distances. Here, the Euclidean distance is defined as,

$$Euclidian\ Distance = \sqrt{\sum_{i}^{N}\left(r_{rs,i} - \hat{r}_{rs,i}\right)^2} \qquad (6)$$

where $r_{rs,i}$ and $\hat{r}_{rs,i}$ are the sensor-derived and modeled subsurface remote sensing reflectance at waveband i, respectively. To assist the L-M optimization in locating the best local minimum, an update-repeat process was used. This procedure began by inverting the r_{rs} spectrum of a given pixel to solve for the in-water optical parameters, depth and bottom albedo coefficients. If this initial inversion achieved a Euclidean distance of $\leq 1.0\times10^{-4}$, the optimal set of model parameters were then used as initial guesses for inverting the set of noise perturbed spectra, $r_{rs}+ \delta r_{rs}$. If, however, the Euclidean distance of the initial L-M fit was greater than this threshold, the procedure entered a 'repeat' stage, where the initial optimal set of model parameters were randomly perturbed by 10% of their value and used as the initial guess for the subsequent inversion attempt. This process was repeated until either the Euclidean distance fell below this threshold, or if this repetition occurred more than four times. In the latter case, the set of optimized values that generated the lowest Euclidean distance was used as the initial guess for inverting the set of noise perturbed spectra. A comparison between this improved method and the standard approach will be presented elsewhere.

A simple pixel-by-pixel land masking procedure was also performed during the inversion process, whereby a pixel is identified as "land" if its R_{rs}(750 nm) > R_{rs}(400 nm).

2.4 Smoothing techniques

The most noticeable artifact in the retrieved bathymetry and bottom albedo images was the amount of impulse (i.e. salt-and-pepper speckling) noise present. Using a median filter would reduce this effect and replace the values of impulse noise pixels with a reasonable estimate; however it would also cause blurring of regions where impulse noise pixels are absent and thereby cause information loss. To limit the blurring of unaffected image regions, we opted for a three step smoothing approach designed to eliminate impulse noise pixels, reduce the magnitude of random (systematic) noise as well as preserving image sharpness. This smoothing approach is as follows: (1) An impulse noise detection algorithm was applied to the image, generating a binary, 'impulse' - 'not impulse', image; (2) an adaptive median filter on these 'impulse' pixels was applied, and; (3) a second order binomial average kernel was applied to all pixels in the image. Steps (1) and (2) could be replaced by a LUM (Hardie and Boncelet, 1993) or center weighted median filters (Ko and Lee, 1991), however for the bathymetry image a more manual and flexible definition of a impulse noise is desired – which can be changed according to the user's prior knowledge. Additionally, step (2) allows the median filter to change size according to the number of other unwanted pixels in the kernel.

For the impulse noise detection algorithm, a 3×3 square pixel region was created and centered on a given pixel of the raw image. The absolute differences between the value of the central pixel and the values of the eight surrounding pixels were then computed. The central pixel was then classified as 'impulse noise' if the differences are greater than a given threshold for more than four of its surrounding pixels. For bathymetry images, this threshold

was set to a value of 2.0 m, whilst for the bottom albedos of sand and seagrass, thresholds of 0.1 and 0.01 were used respectively. Note that this kernel was not centered on pixels that were flagged as land or clouds.

Typically, a 3×3 median filter kernel is used to replace impulse noise pixels, as it finds an estimate from the most immediate surrounds; however each raw image also contained unwanted land, cloud or other impulse noise pixels. Such undesired pixels can heavily contaminate a 3×3 pixel neighborhood, thereby reducing the number of pixels from which the median value is calculated. Thus we have opted for an adaptive approach whereby the kernel size of the median filter is increased if more than 50% of its pixels are undesired (i.e. cloud, land or other impulse noise pixels). Within this approach, the maximum kernel size was set to 15×15, whereby the kernel cannot increase past this size and the median value calculation is forced even if the condition was not met.

The third step of the smoothing approach involved iterating a second order binomial smoother through all pixels of the image (except the edges), whose image kernel is given by equation (7) (Jahne, 2005),

$$Binomial\ Smoother = \frac{1}{16}\begin{bmatrix} 1 & 2 & 1 \\ 2 & 4 & 2 \\ 1 & 2 & 1 \end{bmatrix} \quad (7)$$

Applying this kernel to a given pixel replaced its value with a centrally weighted average of its pixel neighborhood.

The uncertainty products (δH, δB_{sand} and $\delta B_{seagrass}$) were also modified during the adaptive median filtering and binomial smoothing stages. In the former, the uncertainty of a given impulse noise pixel was replaced by that of the selected pixel, whilst in the latter the kernel of equation (7) was convolved through the resultant uncertainty image.

2.5 Tide height correction of bathymetric products

Delineating the changes in depth caused by resuspension and sedimentation from changes in tide heights is an important task in detecting trends and seasonal changes in bathymetry. Ideally, the retrieved bathymetric data are corrected for tidal influences to a common tidal datum such as lowest astronomical tide, LAT. However, water level data measured by *in situ* gauges was not available for the Faure Sill. This prevented direct correction of tidal influences observed in the set of bathymetry images through time (henceforth referred to as bathymetry time series). Two approaches to tide correction were investigated, the first consisting of harmonic tidal analysis and the second based on image analysis.

2.5.1 Harmonic Tidal Analysis

Water height data, above LAT, at five minute intervals were obtained from the Carnarvon tide station (approximately 120 km NW of Faure Sill) from December 2011 to November 2012 – courtesy of the Western Australian Department of Transport. In the harmonic analysis, we followed Burling et al. (2003) and assumed that the tide height is the summation of the M_2, S_2, K_1 and O_1 tidal constituents,

$$height(t) = \bar{h} + \sum_{i=1}^{N} a_i \cos(\sigma_i t + g_i) \qquad (8)$$

where $\bar{h}$ is the mean sea height and a_i, σ_i and g_i are the amplitude (cm), frequency (radians/hour) and phase (radians) of tidal constituent *i*, respectively. The frequencies, σ, of each tidal constituent are known parameters and were obtained from Doodson and Warburg (1941). With $\bar{h}$ set as the mean sea height of the Carnarvon data, equation (8) was used to estimate the water heights at Monkey Mia and Hamelin Pool using: (a) the modeled amplitudes presented by Burling (1998), and; (b) phases derived from harmonic analysis of Monkey Mia and Hamelin Pool tide times. 2 hours and 2 minutes were added (+02:02 hrs) to the tide times of the Carnarvon water height data to estimate the Monkey Mia tide times, as

recommended by the Australian Bureau of Meteorology. Thirty-two minutes were subtracted (-0:32 hrs) from the tide times of the Carnarvon dataset to approximate the Hamelin Pool tide times. Harmonic analysis, in this case, simply involved fitting equation (8) to the approximated tide times using L-M least squares minimization, over multiple time series - each being a three day interval with the HICO overpass being the central point. Finally, the average water height between these two locations (Monkey Mia and Hamelin Pool) was then used to correct for the tide over the Faure Sill.

2.5.2 Image based empirical tidal correction

In the image based approach, an offset is added to each bathymetry image, that normalizes the bathymetry time series to an arbitrary reference depth (tidal datum). This method began by locating those pixels, *P(i,j)*, in the bathymetry time series, *H*(*i*,*j*,*t*), that consistently had a depth of less than three meters through time,

$$H(i,j) \in P(i,j) \quad if \quad H(i,j,t) < 3\,meters \quad \forall\, t = 0, \ldots, N \tag{9}$$

where *i* and *j* represent the spatial coordinates, *t* the time and *N* is the number of bathymetry images in the time series. This constraint effectively excluded any deep water pixel that may have been incorrectly assigned a depth less than three meters through the inversion process at one or more instances in time. Thus the pixels of the set *P*(*i*, *j*) consisted of only shallow water pixels where the signal-to-noise ratio (SNR) was highest and where the retrieved depth was expected to be most accurate. Two medians were then computed: (1) $\widetilde{H(t)}$, the median depth of pixels *P*(*i*, *j*) in each bathymetry image, and; (2) $\widetilde{H_{ref}}$, the median depth of pixels *P*(*i*, *j*) taken across the entire bathymetry time series. This latter median was used as a reference depth to generate an offset value, Δ*H*(*t*),

$$\Delta H(t) = \widetilde{H(t)} - \widetilde{H_{ref}}$$
$$\text{If } \Delta H(t) > \min[H(i,j)]\text{; then } \Delta H(t) = \min[H(i,j)] \quad (10)$$

adding $\Delta H(t)$ to its respective bathymetry image normalized it with respect to $\widetilde{H_{ref}}$, and in so doing minimized the tidal influence across the dataset. In some instances the value of $\Delta H(t)$ was greater than the minimum depth in the bathymetry image, and to avoid over-correction issues $\Delta H(t)$ was set to this minimum.

2.6 Geo-registration

For the purpose of time series analysis in detecting changes in depth, each HICO swath was overlaid on the same raster grid to ensure geospatial consistency through time. This was performed by first geo-referencing each HICO image with the provided geographic lookup tables (GLTs) where an additional rotation was added to orientate north as "up". This was followed by geo-registration where the geo-referenced image was warped by translation/scaling/rotation using at least thirteen ground control points selected from Google Earth™ imagery of Shark Bay. In the absence of accurately registered digital maps of the area, we have assumed the Google Earth imagery to be an accurate reference, noting that a relative, geospatial consistency through time was sought after, rather than absolute geolocation accuracy.

Due to the lack of man-made features in the Shark Bay region, distinct and spatially invariant land features were chosen as ground control points (GCPs). The central position of nine different birridas (see Figure 3) - salty depressions that are either circular, oval or irregularly shaped (Department of Environment and Conservation n.d) – and four other landscape features formed the 13 common GCPs (Figure 3) used in the geo-registration. Additional GCPs that corresponded to roads, distinct sections of rivers, dry inland lakes and tips of islands were also used. Note that these additional GCPs were different for each HICO

swath due to cloud cover and the changing swath orientation and translational drift (see Figure 1).

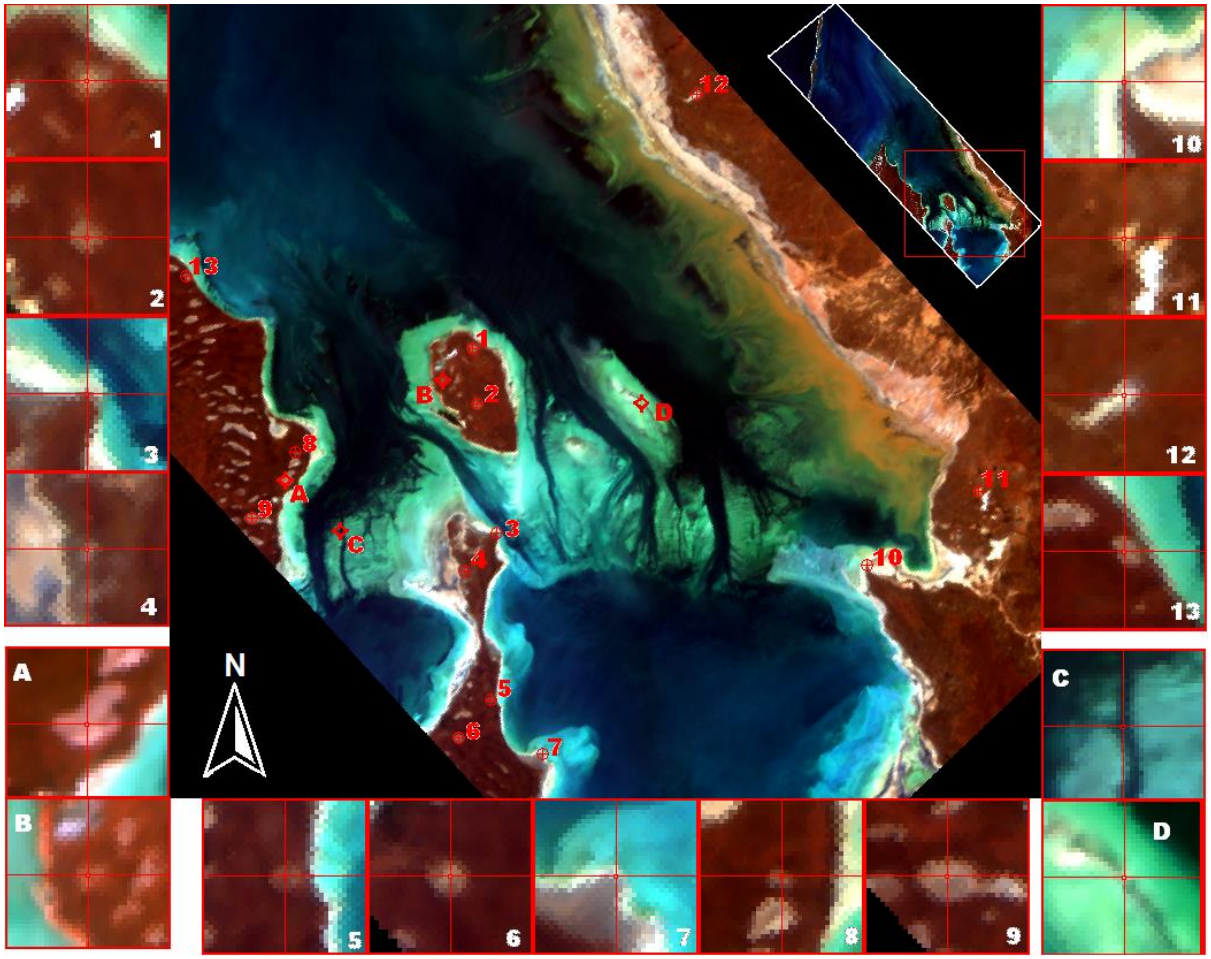

Figure 3: The 13 common ground control points used in the geo-registering of HICO imagery of Shark Bay, Western Australia, and the four test locations for geospatial consistency. The HICO image (19 Nov 2011) displayed has been geo-referenced with the geographic lookup table.

3.0 Results and Discussion

3.1 Evaluation of Tafkaa-6S atmospheric correction

Figure 4 shows the reflectance spectra of two separate pixels through time: a quasi-deep water and shallow submerged sand pixel. The left-hand panels (Figure 4a and 4c) and right-hand panels (Figure 4b and 4d) in this figure show the R_{rs} before and after sun-glint correction, respectively. The reflectance spectra of the shallow submerged sand pixel (Figure

4a) exhibits three spectral artifacts: (1) an upward spectral shift occurring from 400 – 450 nm (e.g. 27 February- and 02 April 2012); (2) negative reflectance values from 400 – 420 nm (e.g. 08 August- and 04 June-2012), and; (3) negative reflectance values beyond 600 nm (e.g. 21 January- and 27 February-2012).

The first spectral artifact, according to Goodman et al. (2008), can be "considered a function of uncorrected sunglint effects" and "attributed to artifact suppression algorithms". The cause of the second spectral artifact is uncertain, however it could arise from an over-estimation of either the radiance of Rayleigh scattering or from the atmospheric aerosol model at the blue wavelength region. This second spectral artifact has been observed in remote sensing reflectance spectra of optically deep water pixels by other researchers (see Fig. 9c in Gao et al., 2000; and Fig. 6b and 7b in Goodman et al., 2003). This spectral artifact was noted specifically for HICO by Moses et al. (2014) and was remedied by assuming very low aerosol loadings when applying Tafkaa-6S. Assuming AOT, CLMVAP, and Ozone values derived from MODIS were best approximations for Shark Bay, the second spectral effect may then be due to the atmospheric and/or aerosol models used within Tafkaa-6S. It is likely the atmospheric and aerosol models used may be sub-optimal for the semi-arid coastal climate of Shark Bay however, improvements to these models is beyond the scope of this work. Further, Goodman et al. (2008) noted that using full geometry implementations of Tafkaa (i.e. with cross-track pointing information) the type of spectral effects seen here might be reduced. The third artifact is more problematic with respect to accurate retrieval of geophysical parameters using the BRUCE model.

When examining Figure 4a, the reflectance spectra of the quasi-deep water pixel on both 21 January 2012 and 27 February 2012 appear to have similar spectral shapes to those of the other dates, with the main difference being a vertical offset/shift. This implies an over-correction of the atmospheric signal that may be due to an over-estimation of one or more

MODIS-derived atmospheric parameters, which were used as inputs to Tafkaa-6S. Indeed, the vertical column water vapor and AOT for these two dates were amongst the highest (see Table 1). After sun-glint correction, the third spectral artifact is removed but accentuates the second spectral artifact (see Figure 4b).

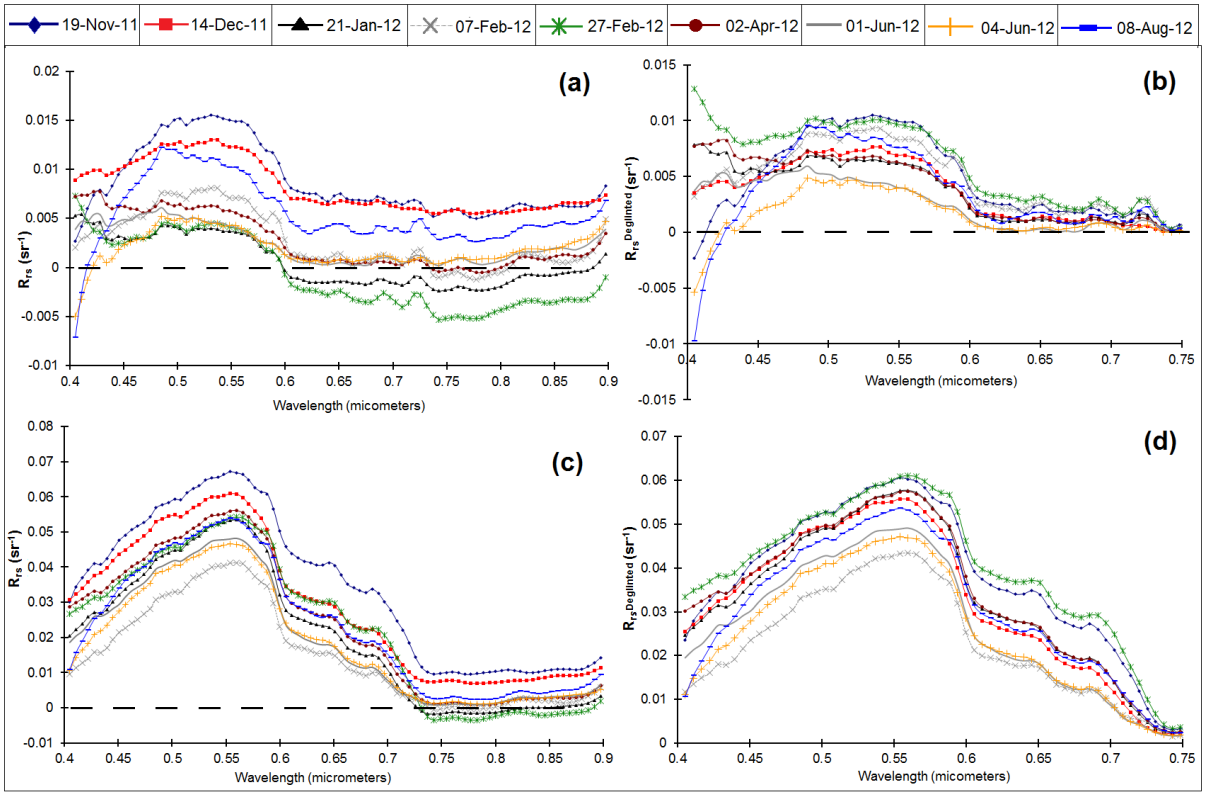

Figure 4: The remote sensing reflectance spectra of a quasi-deep water pixel (a), (25.718 °S/113.978 °E), and a shallow water pixel with a sandy bottom (c), (25.907 °S/113.934 °E), through time. (b) and (d) show the sun-glint corrected R_{rs} spectra of (a) and (c) respectively. Note that the wavelengths past 750-nm are not used in the inversion procedure and are not displayed in (b) and (d).

Analysis of the reflectance spectra of the shallow water pixel (Figure 4c) also shows the occurrence of the three spectral artifacts. However, the magnitude of the reflectance spectra is significantly larger than the magnitude of these spectral artifacts. Moreover these artifacts have marginal impacts across the water penetrating bands between 450 and 600 nm, and as such are deemed less likely to dramatically impair depth retrievals. Negative

reflectances at long wavelengths (third spectral artifact) after Tafkaa's atmospheric correction, was also observed by Goodman et al. (2008) over bright shallow water (sandy substrate) pixels. Goodman et al. (2008), illustrated that this spectral feature does not undermine accurate depth retrievals, as the de-glinting procedure effectively normalizes the reflectance at 750 to low positive values (see Figure 4d).

This comparison has shown the addition of three anomalous spectral artifacts to the remote sensing reflectance spectra after Tafkaa-6S atmospheric correction. The magnitude of these spectral noise are comparable to that of the water-leaving reflectance for deep water pixels, which may lead to inaccurate IOP retrievals. However, as the purpose of this study was to retrieve water column depth, the Tafkaa-derived HICO R_{rs} values over shallow water pixels were deemed suitable in accordance with Goodman et al. (2008).

3.2 Bathymetry retrievals and smoothing techniques

Figure 5 illustrates the step-wise modification of the HICO-derived water column depth product of Shark Bay, 19 November 2011, using the proposed smoothing algorithm. Two cross-sectional profiles are presented, each containing: the raw HICO-derived depth (black curves); pixels classified as impulse noise (red triangles); (c) the depth after impulse noise removal (blue curves), and; the depth after subsequent application of the second order binomial spatial smoother (pink curves). Figure 5 also shows the depth uncertainty profile and its subsequent modification.

The raw depth profiles (Figure 5) demonstrate how impulse noise pixels introduce unrealistic and abrupt changes in the depth product. These pixels were predominantly encountered when the depth of the immediate neighborhood was greater than 4.0 m. Additionally, their uncertainties approached, and at times exceeded 100%, of the actual retrieved depth value. Analysis showed that the R_{rs} spectra of impulse noise pixels whose

depths have been estimated to over 7.0 m resembled that of quasi-optically deep water (e.g. Figure 4a). In such cases, the bottom contribution to the R_{rs} are either weak or non-existent where the geometric depth would be large or precluded by highly absorbing waters. The likely cause for the deeper impulse noise pixels is a low SNR (after atmospheric and sun-glint correction), and where the BRUCE model translates a change in the r_{rs} to large changes in depth (this is explained further in the discussion of Figure 6). The BRUCE model can also compensate for a shallower depth by either increasing the water column turbidity or decreasing the benthic albedo coefficient (darker substrate). This phenomenon creates those impulse noise pixels whose depths are unexpectedly shallower than the surrounding pixels.

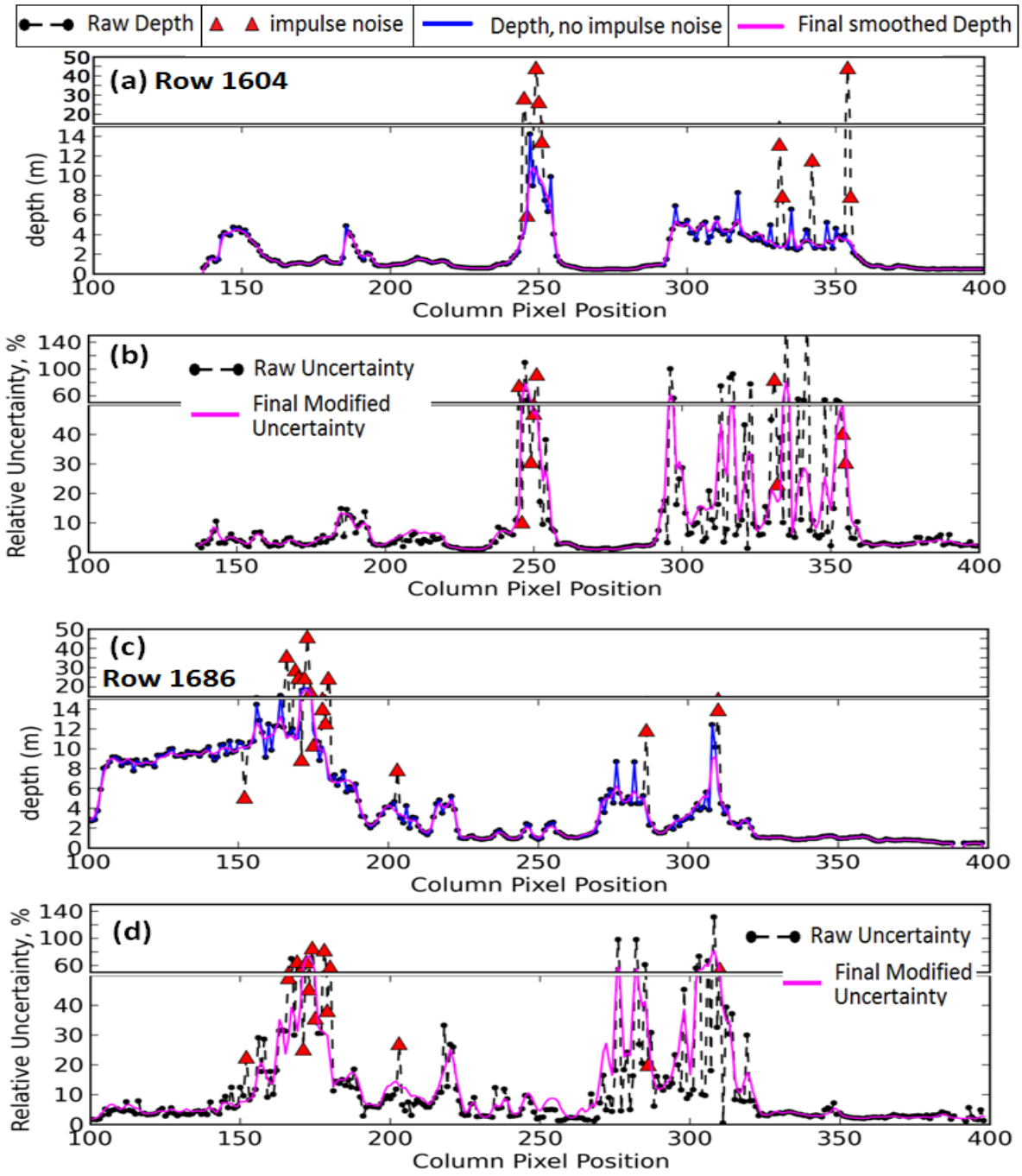

Figure 5: Illustration of the three stage smoothing technique applied to HICO derived depth product of Shark Bay on 19 November 2011. Cross-sectional profiles at row number 1604 (top two panels) and at 1686 (bottom two panels). (a) and (c) contain: the raw depth (black dot-dash); impulse pixels (red triangles); depth product after impulse noise pixel removal (solid blue curve), and; the subsequent smoothed depth product. (b) and (d) are the uncertainty profiles of (a) and (c) respectively, and contain: the initial uncertainty (black dot-dash); pixels identified as outliers (red triangles), and; the final modified uncertainty product (pink).

As shown in Figure 5, the proposed impulse noise detection algorithm and subsequent adaptive median filter approach successfully identified impulse noise pixels and replaced their depth value with a reasonable estimate. Application of a second order binomial smoothing kernel then afforded a reasonable spatial uniformity. The smoothed bathymetry images of Shark Bay from 19-Nov-11 to 08-Aug-12 are displayed in Figure 7, and show a high level of consistency in depth between different timestamps. In the uncertainty inversion approach, proposed by Hedley et al. (2010), the Cholesky decomposition matrix, L, was used to add spectrally correlated noise to the sensor-derived r_{rs} spectra. During per-pixel inversion, the L matrix remained constant with only its magnitude randomly changed. This generated a spectral noise term, δr_{rs}, that is absolute rather than relative to the magnitude of r_{rs}, which thus formed an inverse relationship between $||r_{rs}||$ and its relative uncertainty. In other words, the relative uncertainty in r_{rs} for dark or highly absorbing water pixels will be larger than for bright shallow water pixels. This is illustrated in Figure 6, which shows the pseudo SNR at 550 nm plotted against the relative uncertainty of the retrieved depth. Here, the pseudo SNR was: (a) derived from r_{rs} spectra, i.e. HICO data that has undergone atmospheric, sunglint and air-to-water corrections, and; (b) computed for each pixel in a HICO scene by dividing the average, μ, of each set of 20 noise perturbed r_{rs} spectra at 550 nm by the standard deviation, σ, at this water penetrating wavelength,

$$SNR\ (550\ nm) = \frac{\mu[\{r_{rs}(550) + \delta r_{rs}(550)\}_{i=1\ldots20}]}{\sigma[\{r_{rs}(550) + \delta r_{rs}(550)\}_{i=1\ldots20}]} \qquad (11)$$

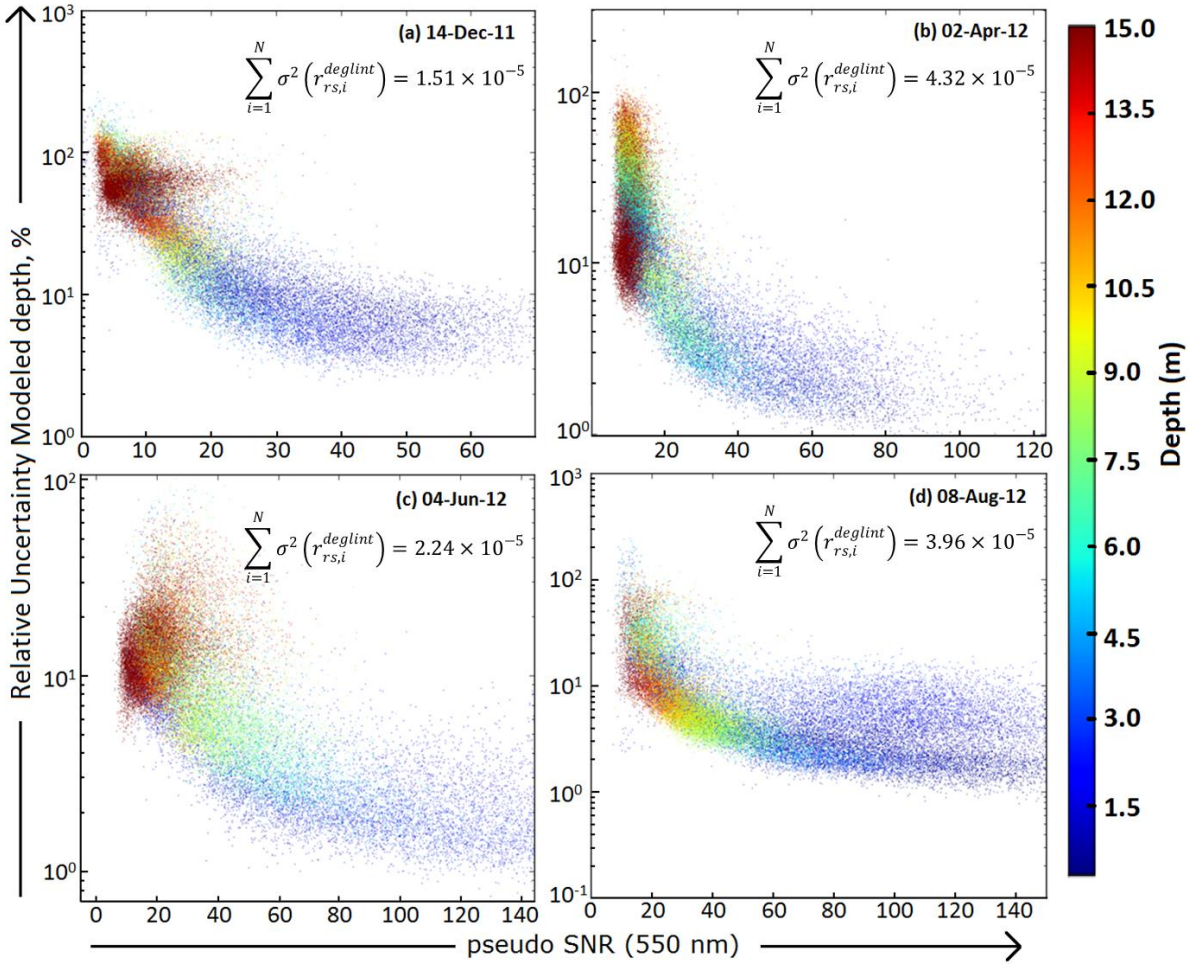

Figure 6: Relative uncertainty of the retrieved depth vs. pseudo SNR at 550 nm, obtained from HICO images of Shark Bay on (a) 14-Dec-11; (b) 02-Apr-12; (c) 04-Jun-12, and; (d) 08-Aug-12. Note: (1) vertical axes are displayed in logarithmic form; (2) 35 000 random data points, with depth > 0.3 m, were presented for each panel, and; (3) the summed spectral variance, taken from the deep water region of the given HICO $r_{rs}^{deglinted}$ image are also presented.

Figure 6 shows a non-linear relationship between the pseudo SNR and the relative uncertainty of the retrieved depth of four HICO scenes of Shark Bay. From Figure 6, we can see that when the SNR is above 20, the relative uncertainty of the retrieved depth is less than 10%. This is an adequate outcome, and analysis of the entire HICO time series for Shark Bay

showed that on average 89% of pixels with a retrieved depth less than 5 m had a SNR greater than 20. This average decreases to 74% for pixels whose depths ranged between 5 and 10 m, and to 49% for pixels with a retrieved depth greater than 10 m. Below a SNR of 20, the relative uncertainty in the retrieved depth drastically increases, in most cases to greater than 100%. Such high uncertainties mainly occur for pixels with a retrieved depth greater than 8 meters.

This behavior can be attributed to the absolute noise term added during the inversion; where, as the SNR decreases below 20, the magnitude of δr_{rs} starts to become comparable to $\|r_{rs}\|$. Given the exponential relationship between r_{rs} and depth in the shallow water model; the BRUCE model translates this perturbation of r_{rs} to large changes in depth, and hence why the retrieved depth varies so greatly within the set of 20 noise perturbed r_{rs} spectra for low SNR pixels – e.g. the deeper impulse noise pixels observed in Figure 5. Conversely, over bright substrates, where $\|\delta r_{rs}(\lambda)\| \ll \|r_{rs}(\lambda)\|$, δr_{rs} is translated to smaller changes in depth. These relationships are demonstrated in Figure 5, where pixels with a modeled depth less than 6 m generally had a relative depth uncertainty of less than 10%, and where this relative uncertainty would at times increase with depth.

Figure 6 also shows that when environmental noise is included, arising from atmospheric, sun-glint and water-to-air interface corrections, the SNR of HICO – which was initially estimated at approximately 200 at 550 nm (see Lucke et al., 2011) - drops to less than 150 for most cases. This corresponds to an increase in the noise component by a factor of ≥ 1.3. While this is a modest increase, it does illustrate the importance of accurately removing contaminating signals in a bid to avoid non-uniqueness issues, which lead to higher uncertainties in the retrievals of depth.

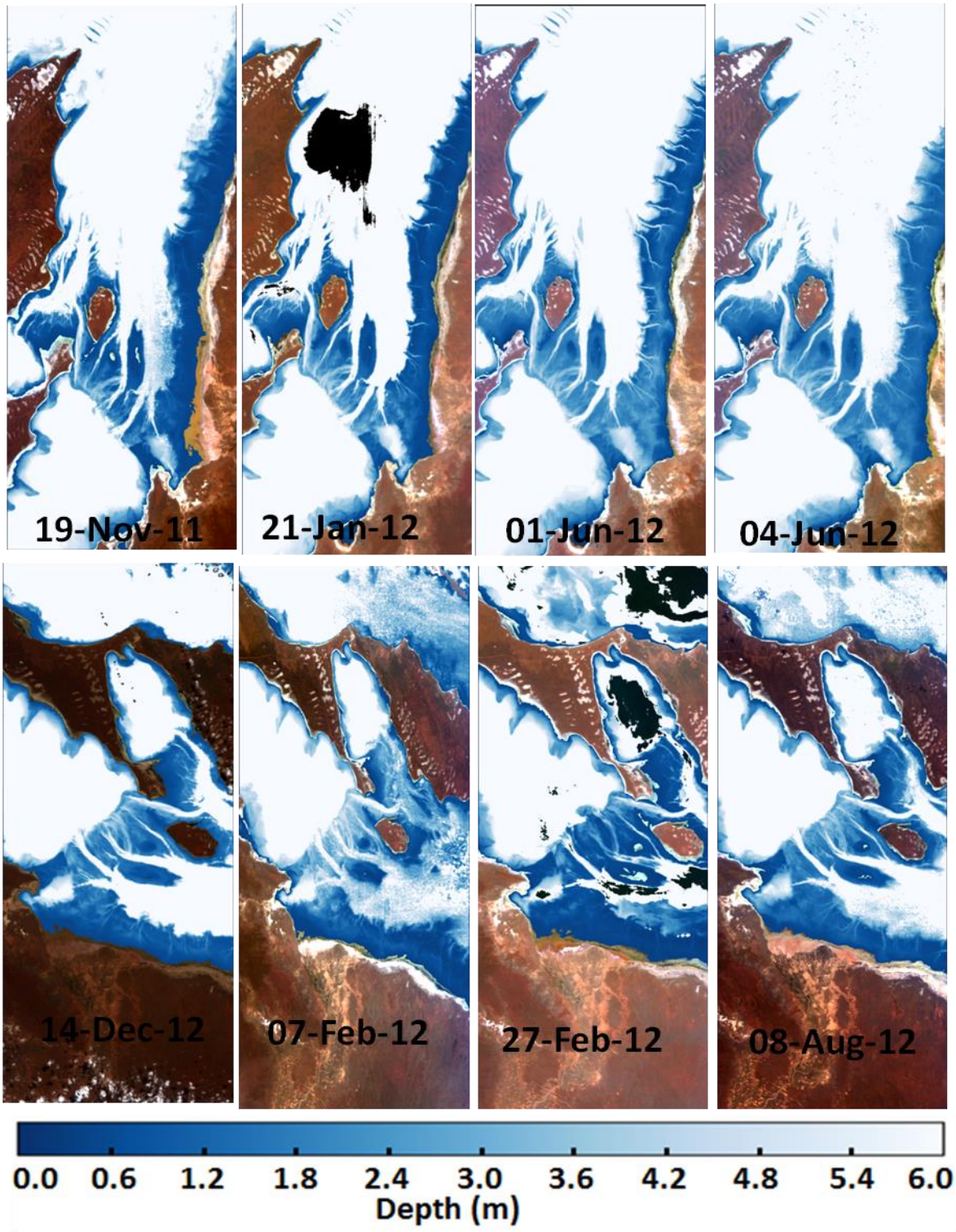

Figure 7: Smoothed bathymetry images (before geo-referencing) derived from HICO imagery of the Shark Bay region, from 19-Nov-11 to 08-Aug-12. Note: for simplicity the bathymetry image of 02-Apr-12 is not displayed; black water pixels (e.g. 12-Jan-12 and 27-Feb-12) had $R_{rs}(750) > R_{rs}(400)$ and were not processed, and; blue and white represent shallow and deeper areas respectively.

3.3 Tide corrections

3.3.1 Harmonic Tidal Analysis

Removing the influence of tide is an important task in delineating changes caused by resuspension and sedimentation from changes in tide heights, particularly since tides can form a significant portion of the variance observed in raw bathymetry products (Egbert and Erofeeva, 2002).

The harmonic tidal analysis begins by extracting the phases of the major tidal constituents from time-adjusted (+02:02 Hrs and -0:32 Hrs) Carnarvon tide data (Figure 8a). The correlation coefficients of the curves in Figure 8a are given in Table 2 and with $r^2 > 0.96$ for all dates, demonstrates high confidence in the values of the modeled phases. The slight differences between the observed and modeled tide heights in Figure 8a are likely due to wind induced waves, which do not affect the accuracy of the retrieved phases. Applying these phases with the respective amplitudes taken from Burling et al. (2003), generates modeled tide curves for Monkey Mia and Hamelin Pool as illustrated in Figure 8b for 14 December 2011.

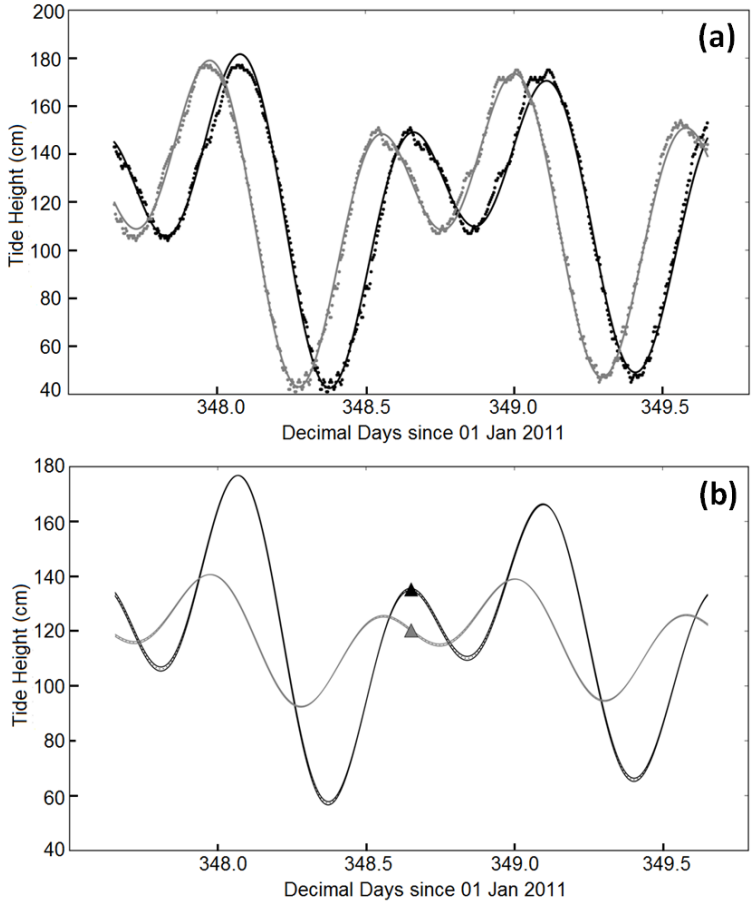

Figure 8: Harmonic tidal analysis for a 3 day interval centered on the HICO overpass of 14 December 2011: (a) Time adjusted Carnarvon tide height data for Monkey Mia (+2:02 hrs - Black dots) and Hamelin Pool (-0:32 hrs - Grey dots) overlaid with the respective modeled tide curves using equation (8); (b) Modeled tide curves for Monkey Mia (Black line) and Hamelin Pool (Grey line). The triangles in (b) display the modeled water level height at the time of the HICO overpass at Monkey Mia and Hamelin Pool.

One and a half day intervals about the HICO overpass were used to compute the phases of the major tidal constituents as these produced higher correlation coefficients than an expanded time series. The modeled tide heights and their uncertainty at the time of each HICO overpass for Monkey Mia, Hamelin Pool and Faure Sill are given in Table 2. The Faure Sill, being a shallow water region containing several narrow water channels (of depths greater than 6 m) exhibits complex tidal harmonics (Burling et al., 2003). Modeling these harmonics are beyond the scope of this paper, however previous research has shown that the

Faure Sill diminishes the amplitudes and creates lag in the phases of the tidal constituents (Burling et al., 2003). The net result is a lower tidal height and range in Hamelin Pool than in Monkey Mia. This is observed in the modeled tide data (Table 2), where the tide range at Monkey Mia and Hamelin Pool are 81.14 cm and 64.71 cm respectively. Additionally, Table 2 suggests little variation in the expected water level height between successive HICO overpasses; evident by the modeled tide ranges of less than 1 m and a standard deviation of tide heights less than 30 cm for Monkey Mia and Hamelin Pool. Indeed a tide height range of approximately 1 m over Shark Bay has been noted by Walker et al. (1988) and modeled by Burling et al. (2003).

Table 2: Modeled tide heights (cm), above LAT, during each HICO overpass time for Monkey Mia, Hamelin Pool and the Faure Sill. Also present are the: standard deviation and range of these tide heights, and; correlation coefficients of the tide height curves used to extract the M_2, S_2, K_1, and O_1 tide constituent phases from the time adjusted Carnarvon data.

Date and Time (WST)	Monkey Mia		Hamelin Pool		Faure Sill
	r^2	Modeled tide height (cm)	r^2	Modeled tide height (cm)	Modeled tide height (cm)
19-Nov-2011, 1632 hrs	0.983	124.28 ± 0.01	0.978	114.06 ± 0.04	119.17 ± 0.05
14-Dec-2011, 1539 hrs	0.991	135.21 ± 0.22	0.995	120.23 ± 0.18	127.72 ± 0.40
21-Jan-2012, 1538 hrs	0.983	112.43 ± 0.35	0.991	132.98 ± 0.18	122.70 ± 0.54
07-Feb-2012, 1722 hrs	0.988	115.25 ± 0.44	0.994	133.82 ± 0.19	124.54 ± 0.63
27-Feb-2012, 0940 hrs	0.981	95.19 ± 0.02	0.991	121.92 ± 0.02	108.55 ± 0.05
02-Apr-2012, 1035 hrs	0.966	125.91 ± 0.18	0.983	128.12 ± 0.22	127.01 ± 0.40
01-Jun-2012, 1038 hrs	0.973	173.39 ± 0.18	0.990	127.11 ± 0.07	150.25 ± 0.25
04-Jun-2012, 0932 hrs	0.990	165.61 ± 0.10	0.994	149.56 ± 0.06	157.58 ± 0.15
08-Aug-2012, 1625 hrs	0.962	118.60 ± 0.31	0.988	92.99 ± 0.22	105.79 ± 0.54
Standard deviation of tide heights (cm)	N/A	26.55	N/A	19.30	20.24
Tide range (cm)	N/A	81.14 ± 0.20	N/A	64.71 ± 0.28	69.04 ± 0.69

Although the modeled tide heights at Monkey Mia and Hamelin Pool appear reasonable based on evidence from the literature, the estimated tide heights over the Faure Sill can be subject to large errors. These errors arise when averaging the tide height between Monkey Mia and Hamelin Pool, which may over simplify the complexity of the shallow water tidal harmonics present over the Faure Sill. In this region, shallow water tidal constituents may cause constructive or destructive interference with the M_2, S_2, K_1, O_1 harmonics, increasing or decreasing the tide height respectively (Doodson and Warburg, 1941). However, with the absence of accurate three-dimensional tide modeling (e.g. Burling et al., 2003), adopting the average is the most pragmatic approach.

3.3.2 Image based tide correction

To gauge if a tidal signal exists in the HICO derived bathymetry dataset, the predicted tide heights at Monkey Mia (taken from Table 2) were plotted against the median HICO derived depth of the shallow water region on the northern side of Faure Island (Figure 9). This island is approximately in line with Monkey Mia, and as modeled by Burling (1998), experiences very similar tidal harmonics. Figure 9 shows a strong positive correlation (R^2 = 0.90) between the predicted tide heights and the HICO derived bathymetry prior to tide correction, that is, the bathymetry increases with the tide height. Note that a 1:1 line was not expected because: (a) the predicted tide heights are given above LAT; (b) Burling (1998) obtained a normalized RMS of 7% between the predicted and observed tide heights at Monkey Mia with the modeled tidal amplitudes and phases, and; (c) potential random offsets in the bathymetry data caused by sub-optimal atmospheric/sun-glint/air-water interface corrections. Despite this Figure 9 implies that the variation in depth between HICO derived bathymetry images are related to tide, and not solely due to random offsets.

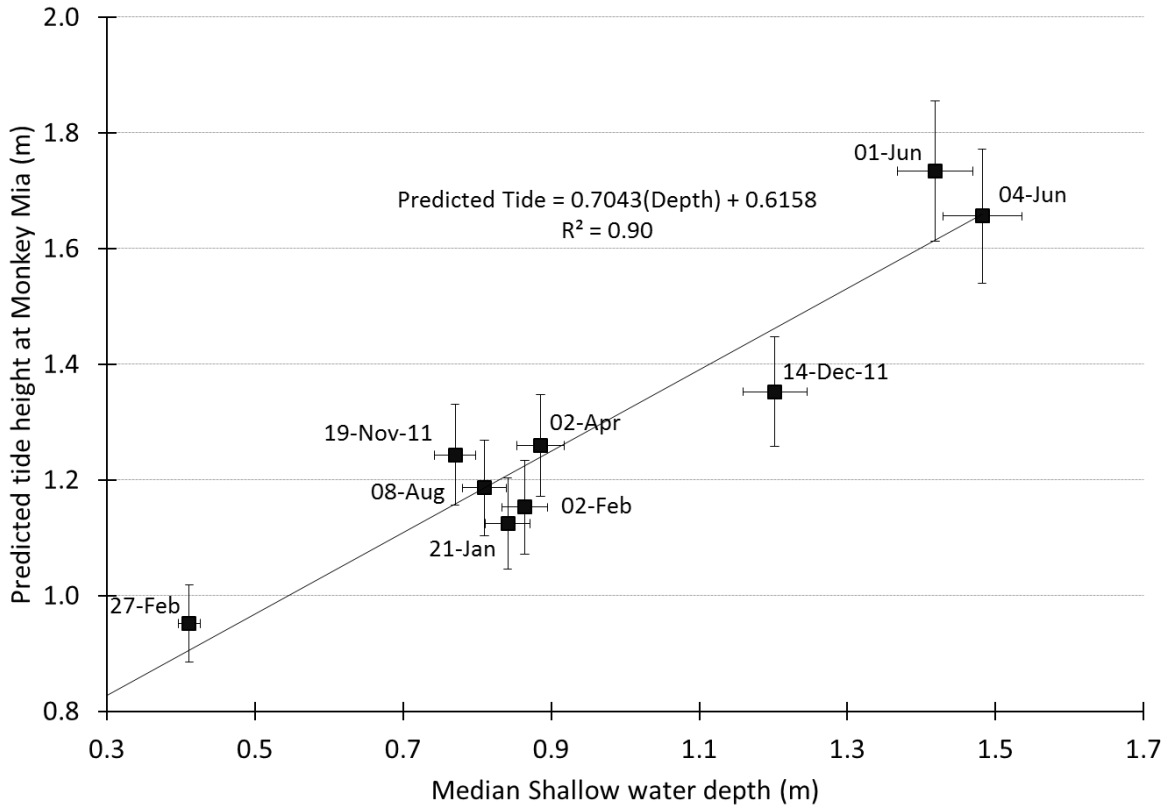

Figure 9: Predicted tide heights at Monkey Mia against the median depth of the shallow water pixels surrounding the northern section of Faure Island. The predicted tide heights were taken from Table 2, whilst the median shallow water depths were taken from HICO derived bathymetry prior to tide correction. The nine data points represent the nine HICO scenes.

The image based tide correction technique is illustrated in Figure 10a. This figure shows the median shallow water depth, $\widetilde{H(t)}$, computed for each HICO image of Shark Bay. The black horizontal line is the reference depth, $\widetilde{H_{ref}}$, from which the offset of each bathymetry image is calculated. The reference depth in this case is the median water depth computed from all nine HICO scenes. Note that if tide data of the region of interest is available, then the mean water level height or the lowest astronomical tide may instead be used as the reference depth.

How well the image based and harmonic analysis techniques minimize the tidal influence across the bathymetry time series was tested by computing the standard error in the

means (SEM). Here, the mean represents the average depth of the shallow water pixels, $<H(t)>$, of each bathymetry image in the time series. Note that applying a tide correction technique to the bathymetry dataset would ideally correct water height variations to a reference depth, and hence yield a SEM near zero. Table 3, shows $<H(t)>$ and the SEM for the uncorrected, image based and harmonic analysis corrected bathymetry images.

Table 3: The mean depth of the shallow water pixels, $<H(t)>$, for each HICO derived bathymetry image. The standard error in the means (SEM) of the uncorrected, image based and harmonic tide correction techniques are also presented.

Tide method	19-Nov-11	14-Dec-11	21-Jan-12	07-Feb-12	27-Feb-12	02-Apr-12	01-Jun-12	04-Jun-12	08-Aug-12	SEM
Uncorrected	0.91	0.91	1.13	1.41	0.80	1.02	1.42	1.38	1.34	0.24
Image based correction	1.26	1.20	1.26	1.56	1.20	1.24	1.13	1.20	1.17	0.12
Harmonic analysis correction	-0.29	-0.36	-0.10	0.16	-0.28	-0.25	-0.08	-0.20	0.28	0.22

As indicated in Table 3, tidal influences over Shark Bay exhibit a SEM of 24 cm with a tidal range of 62 cm. The tidal range is consistent to that modeled using the harmonic tidal analysis (Table 2). However, the harmonic analysis tide correction method did not significantly reduce the variability between the bathymetry images, having also overcorrected the depth of the shallow water pixels as noted by the negative averages displayed in Table 3. These results suggest that tide correction based on harmonic analysis is inaccurate and does not adequately represent the tidal harmonics encountered over the Faure Sill. In contrast, the image based tide correction approach produces a bathymetry times series with an SEM of 12 cm, indicating that the variations due to tide have at least been minimized. Note that the reason the image based tide correction did not generate an SEM of zero is due to the inclusion of the constraint that forces $\Delta H(t)$ to equal the minimum depth (see equation 10) –

for some images – to avoid overcorrection. Thus not all bathymetry images were fully normalized to the imposed reference depth. Figure 10b and 10c show histograms of the depth of the shallow water pixels for each bathymetry image, before and after empirical tide correction, and illustrate the normalization achieved by this method. It should be noted that the corrected depth values obtained from this empirical method are relative to an arbitrary reference depth, rather than an absolute tide datum such as LAT.

These results suggest that unless the local tidal dynamics of the region of interest are well characterized, large errors can arise when using tide data recorded at distant tide stations. The lack of *in situ* tide data in close proximity to the region of interest is a constant issue faced for the majority of remote and inaccessible regions for remote sensing studies. Although global tide models are in existence (e.g. Finite Element Solution 2012, Lyard et al., 2006 ; Topex Poseidon crossover solution 7.2, Egbert and Erofeeva, 2002), their spatial resolutions are coarse (ranging from 1/16° to 1/4° longitude and latitude) and do not extend to semi-enclosed embayment's such as Shark Bay. The image based tide correction circumvents the need for a historic tide dataset and eliminates errors from tide models. Although this approach does require at least two bathymetry images of the region of interest at different times, it is the most pragmatic and easiest to implement. Future research would be to compare the empirical tide correction results with estimates obtained from a harmonic analysis whose tidal constituents are derived from high resolution remote sensing imagery, as presented by Mied et al. (2013).

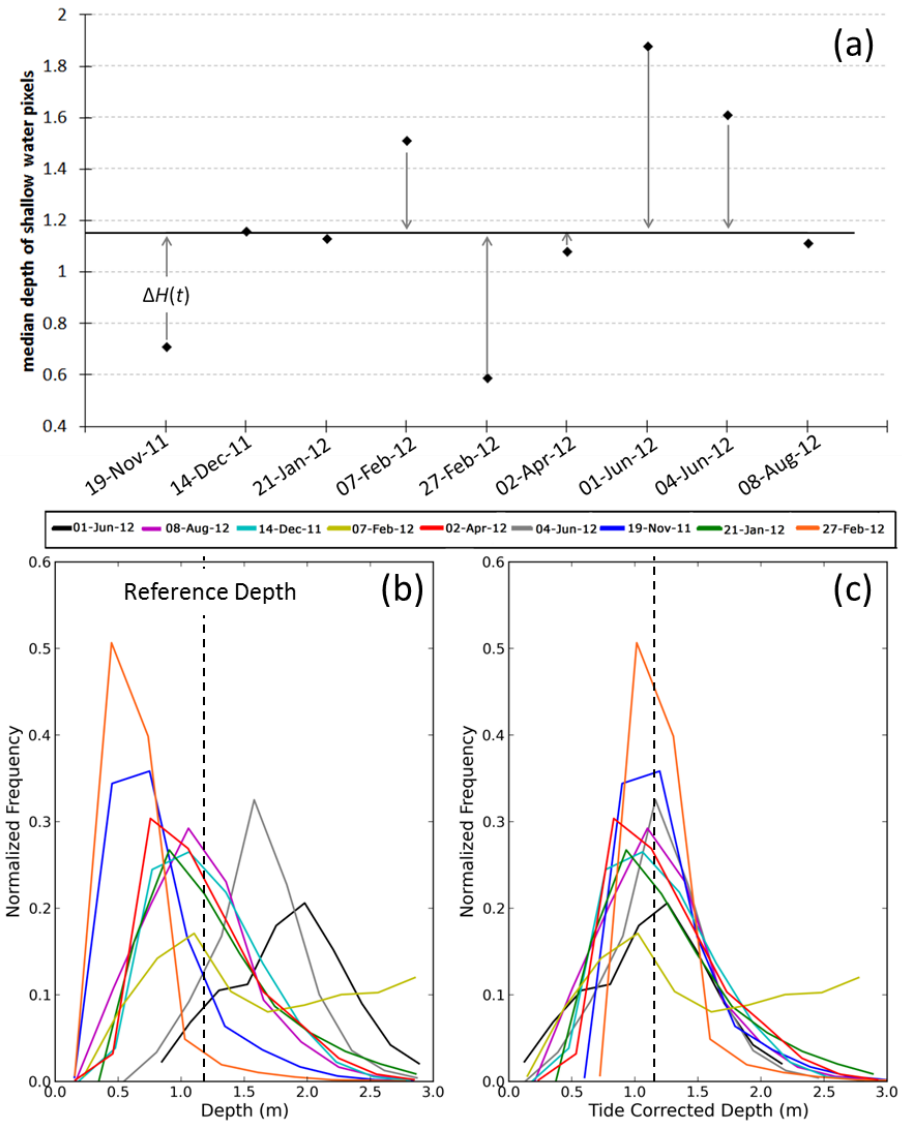

Figure 10: (a) illustration of the empirical tide correction technique applied to the HICO dataset of Shark Bay. The horizontal black line represents the reference depth. Histograms of the depth of shallow water pixels (less than 3 m depth) before (b) and after tide correction (c).

3.4 Geo-registration

To test the geo-spatial consistency, the spatial 'pixel drift' of four test pixels was analyzed between HICO images. Pixels A, B, C and D, displayed in Figure 3, correspond to different land and seascape features, specifically: A and B are pixels within the birradas (described in section 2.3) on the Peron peninsula (25.918 °S/113.737 °E) and Faure Island (25.838 °S/113.862 °E), respectively; C is an intersection point of a distinct and seemingly

invariant water channel on the Faure Sill (25.959 °S/113.779 °E) and; D is the southernmost tip of Pelican Island (23.854 °S/114.019°E). A seascape feature (pixel C) was also included because the majority of GCPs were on the coastal regions surrounding the Faure Sill, and solely choosing test points near these GCPs may bias the result. Additionally, the area surrounding pixel C appeared in both true color and bathymetry imagery to be invariant through time as expected by the qausi-stable nature of Shark Bay's geology.

The Euclidean distance was used to measure the drift of a given test pixel from its reference position,

$$Distance\ (degrees) = \sqrt{\left(\vartheta(A_r) - \vartheta(A_i)\right)^2 + \left(\varphi(A_r) - \varphi(A_i)\right)^2}$$
$$Distance\ (km) = \frac{Distance\ (degrees)}{0.0009\ °} \times \frac{100\ m}{1000\ m\ per\ km} \quad (12)$$

Where $\varphi(A_r)$ and $\vartheta(A_r)$ are the latitude and longitude coordinates for test pixel A in an arbitrary reference image, and $\varphi(A_i)$ and $\vartheta\ (A_i)$ are the latitude and longitude coordinates for test pixel A on subsequent HICO images. We set the HICO image of Shark Bay captured on 19 November as the reference image, and as such the Euclidean distances from equation (12) are relative measures but still illustrate geo-spatial consistency through time. Note that these Euclidean distances were converted to kilometers for ease of interpretation, and are presented in Figure 11.

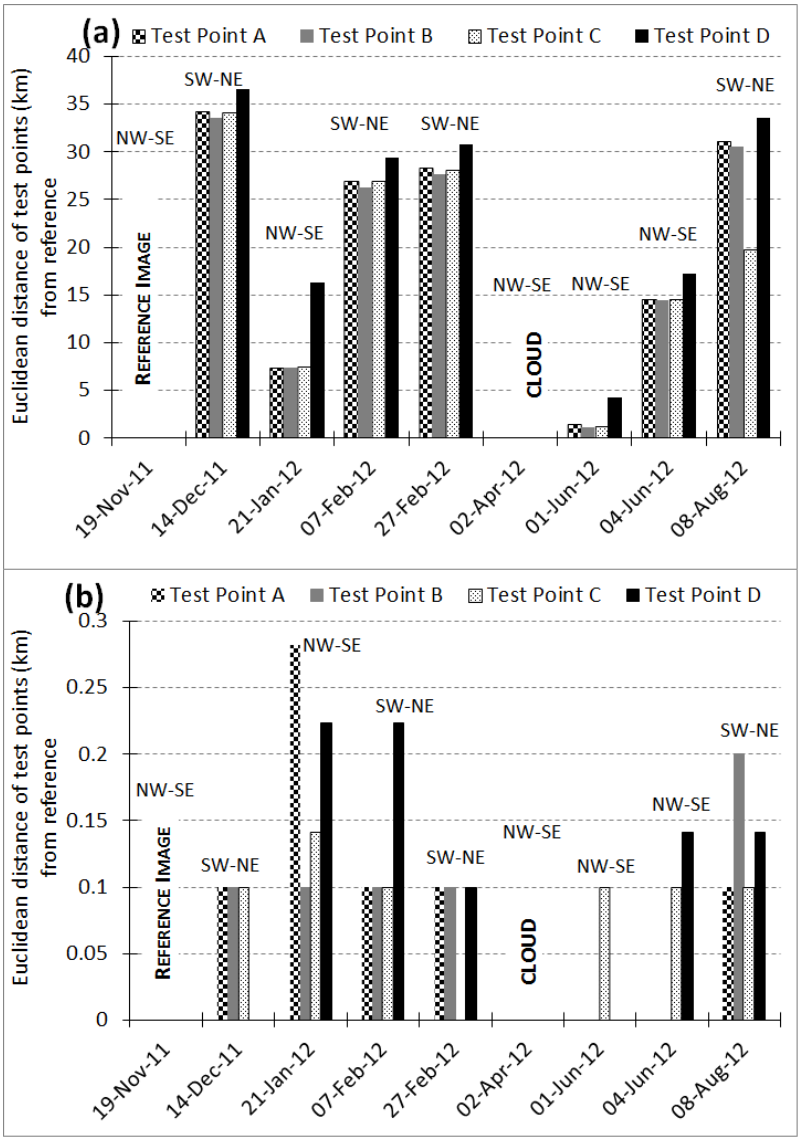

Figure 11: Geo-spatial consistency of each HICO image of Shark Bay, relative to 19 November 2011, after (a) Geo-referencing using the provided GLT files, and (b) subsequent Geo-registration using the ground control points. NW-SE and SW-NE refers to the HICO swath orientation.

Figure 11a shows that simply geo-referencing a HICO swath with the provided GLT can generate geo-spatial inconsistencies greater than 10 km. The largest geo-spatial inconsistency is encountered when the scene is imaged with different swath orientations. For example, the reference image had a NW-SE orientation whilst the images on the 14 December 2011, 7 February, 27 February, and 8 August 2012 had a SW-NE orientation and where the test pixels encountered drifts greater than 20 km from their reference positions

(Figure 11a). In contrast, those dates that were imaged with the same swath orientation (21 January, 1 June, 4 June 2012) exhibited much lower geospatial inconsistencies (< 17 km). Such large relative geospatial displacements will introduce significant errors into change detection analysis, where a change in the geophysical parameter of a pixel is likely due to an evaluation at different locations rather than a temporal change (Townshend et al., 1992). By performing a series of mis-registration simulations on Landsat imagery, Dai and Khorram (1998) showed that a geolocation accuracy of less one fifth (<0.20) of a pixel is needed to detect 90% of real temporal changes. For HICO this equates to achieving 20 m geolocation accuracy.

Manual geo-registration using GCPs taken from Google Earth™ imagery significantly improved the geospatial consistency, where the test pixels were now within 300 m of the reference pixels (Figure 11b). However, this geospatial consistency is still relatively large compared to the 100 x 100 m HICO pixel footprint. Furthermore, this result is poor compared to other operational satellites, such as MODIS and MERIS both of which achieve sub-pixel geolocation accuracies of ~50 m (Wolfe et al., 2002) and 77 m (Bicheron et al., 2011), respectively and whose ground sampling distance are at least twice as much as that of HICO. This highlights the need for an improved HICO geolocation algorithm that will increase the geolocation accuracy of the resultant GLTs and/or an improved method of using GCPs for subsequent geo-registration. The manual geo-registration employed here has proved troublesome due to: (a) the slight translational drift of the HICO swath, which prohibits the use of a consistent set of GCPs; (b) the amount of GCPs needed to achieve a geo-spatial consistency of less than 300 m, and; (c) cloud cover, which when present will compromise the accuracy of the geo-registration.

Fortunately, since the commencement of this research, and as part of the transition of HICO data to NASA, the Naval Research Laboratory (NRL) has improved the geolocation

accuracies of the provided GLTs to 200-300 m. This improved HICO data is now available through NASA's Ocean Biology Processing Group's data portal (http://oceancolor.gsfc.nasa.gov/cgi/browse.pl?sen=hi).

3.5 Change detection

The ability to detect change in a geophysical parameter from multi-temporal remotely sensed imagery is a key outcome in ecosystem monitoring (Coppin et al., 2004). However, literature on detecting change above the uncertainty of multi-temporal datasets is sparse, with exception of Shi and Ehlers (1996) and Hester et al. (2010). This section will assess this ability using the HICO-derived, tide corrected, bathymetry dataset. To this end, it is assumed that each geo-registered bathymetry image has sufficient geolocation accuracy to assess temporal change. A two sample, per-pixel, *t*-test was used to accept or reject the null hypotheses of equal depth (i.e. no change) between pixels (i, j, t_1) and (i, j, t_2). As described in section 2.3, the retrieved depth and its uncertainty were the average and standard deviation, respectively, calculated from a set of 20 noise-perturbed spectra. This is analogous to performing a *t*-test on two independent sample means, assuming unequal variance, both with a sample size of 20. Here, the upper and lower tail of the Student's *t* cumulative distribution function at the calculated *t* statistic and degree of freedom are used to compute the *p* value. The null hypothesis of "no change in depth" is rejected for pixels with $p < 0.05$ (5% significance level).

Figure 12 shows empirically tide corrected bathymetry profiles at row number 1686 for each geo-registered bathymetry image. The uncertainty of the retrieved depth is overlaid around the average depth. This figure illustrates that for shallow waters, of depth less than 6 m, the inversion routine presented can retrieve consistent depths through time – even in the presence of sub-optimal atmospheric correction. However, as the retrieved depth increases, so

does its temporal variability, as illustrated by the quasi-deep water pixels of the Faure Sill channels A and B in Figure 12. This temporal variability is unlikely caused by natural phenomena, and is more likely the result of variable quality of atmospheric correction and shallow water model inversion. As noted in Section 3.1, the magnitude of spectral noise introduced to R_{rs} from atmospheric correction becomes comparable to the reflectance signal as the geometric depth increases. As such, this spectral noise coupled with sun-glint correction would decrease the accuracy in the retrieved depth over quasi-deep water more than it would for shallow water pixels and effectively creates the observed temporal variability in deep water pixels.

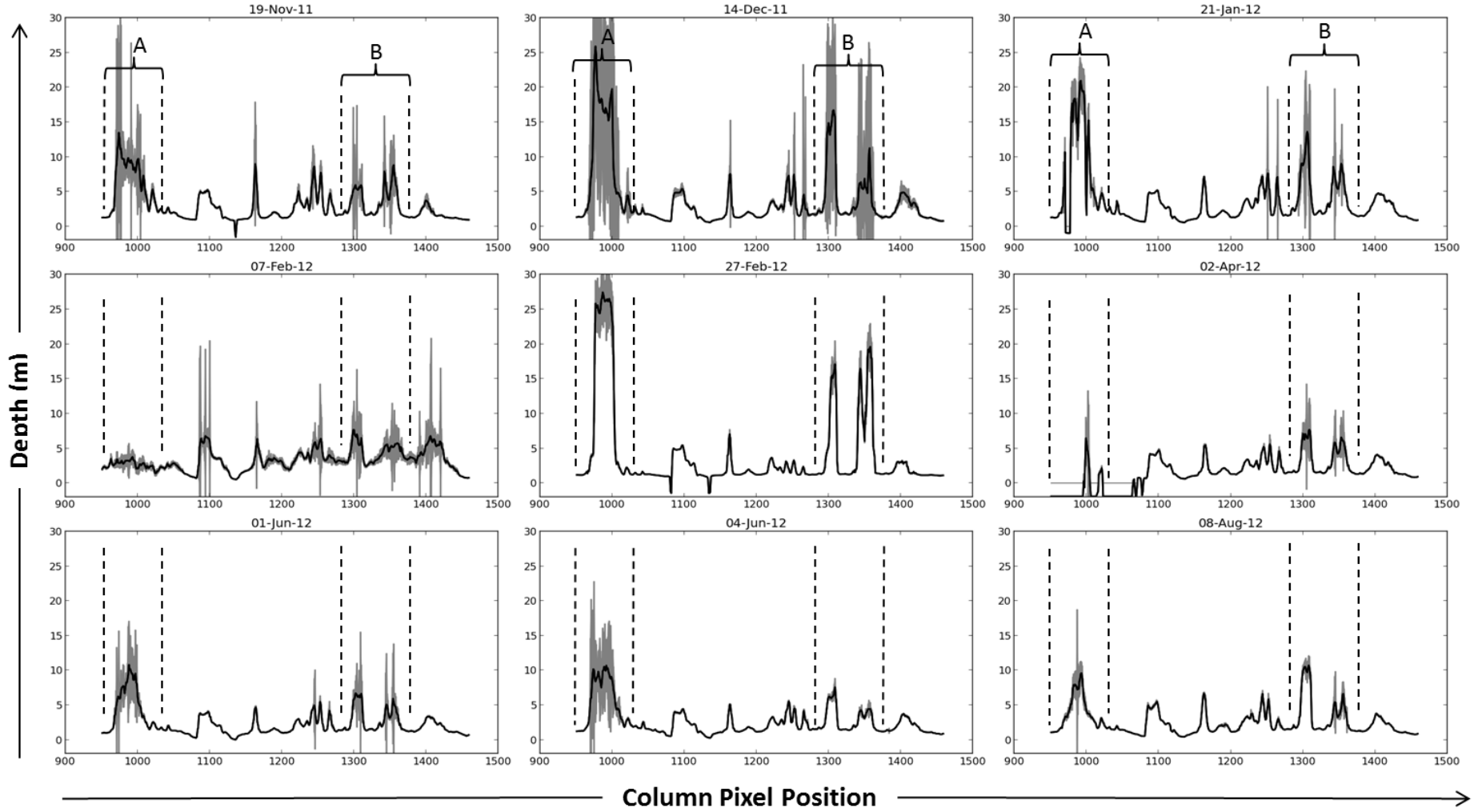

Figure 12: Cross-sectional depth profiles of the Faure Sill, at row 1686, taken from geo-registered HICO derived bathymetry images. The solid black line and grey envelope surrounding it represents the retrieved depth and its uncertainty respectively. Highlighted are two sets of deep water channels, A and B, located at column positions 950-1050 and 1280-1380 respectively. The depth of these channels show high temporal variability, the cause of which is discussed in the text.

Despite the normalization of the bathymetry dataset to a common depth; changes unrelated to tide are expected due to the frequent movement of tidal sandbanks across the Faure Sill. Figure 13 shows changes in the HICO-derived, tide corrected bathymetry across the Faure Sill between the dates of: (a) 14 December 2011 and 21 January 2012; (b) 21 January- and 27 February-2012; (c) 27 February- and 04 June-2012 and; (d) 04 June- and 08-August-2012. In this figure, pixels that observed a change had: (1) a difference in depth greater than the baseline variability, and; (2) a *p* value less than 0.05 (5% interval) at the calculated degree of freedom. Otherwise pixels were classified as having 'no change' and displayed as grey. Here, we define the baseline variability as the residual random fluctuations within the tide corrected bathymetry dataset. Recall that the SEM of the image-based tide corrected bathymetry dataset was 0.12 m (see Table 3). Hence, the bathymetry varied on average by 12 cm between each successive timestamp. We set the baseline variability to equal three times the SEM (i.e. 0.36 m), which would encompass: random offsets in depth due to imperfect atmospheric/sun-glint/air-to-water interface corrections, and; imperfect tide normalization. Therefore any changes in depth greater than the baseline variability of 0.36 m, which are statistically significant with regards to the uncertainty, are plausible and not due to random depth fluctuations caused by corrections performed in the processing.

The change detection analysis shown in figure 13 does not include the bathymetry images on 7th February and 2nd April 2012, as the bathymetry profiles of these dates (see Figure 12) appear inaccurate. This is evident from the derived depth values of channels A and B when compared to the other profiles. Furthermore these two bathymetry images were included (results not presented here), the change detection analysis afforded significant, yet unrealistic changes in depth across the Faure Sill. Additionally, deep-water pixels were flagged in figure 13, due to their temporal variability as noted in figure 12.

For the purpose of change detection, separate image based tide corrections were performed for the different regions of Shark Bay, shown by the dashed magenta regions in Figure 13a. These regions were: (1) the eastern and western shallow areas of Hamelin Pool, and: (2) the Wooramel bank containing water channels orientated perpendicular to the coast. These two additional tide corrected subsets were merged to the tide corrected bathymetry dataset of the Faure Sill (Section 3.3.2) to form a complete tide corrected bathymetry image of lower Shark Bay for each HICO overpass. This latter dataset was used to assess the temporal changes in depth with the method described above.

Separate tide correction over Hamelin Pool and the Wooramel bank were performed to take into account the differing tidal variations across the Shark Bay region. For instance, the tidal regime at Hamelin Pool is particularly complex in which the astronomical tide accounts for only 15% of the variation in water height (Burne and Johnson, 2012). Over this enclosed embayment, the mean sea-level varies in an irregular manner due to seasonal winds. Specifically southerly winds, that during summer, when they are more persistent and strongest, act to reduce the mean sea level by approximately 50 cm compared to that in winter when the southerly winds subside (Burne and Johnson, 2012).

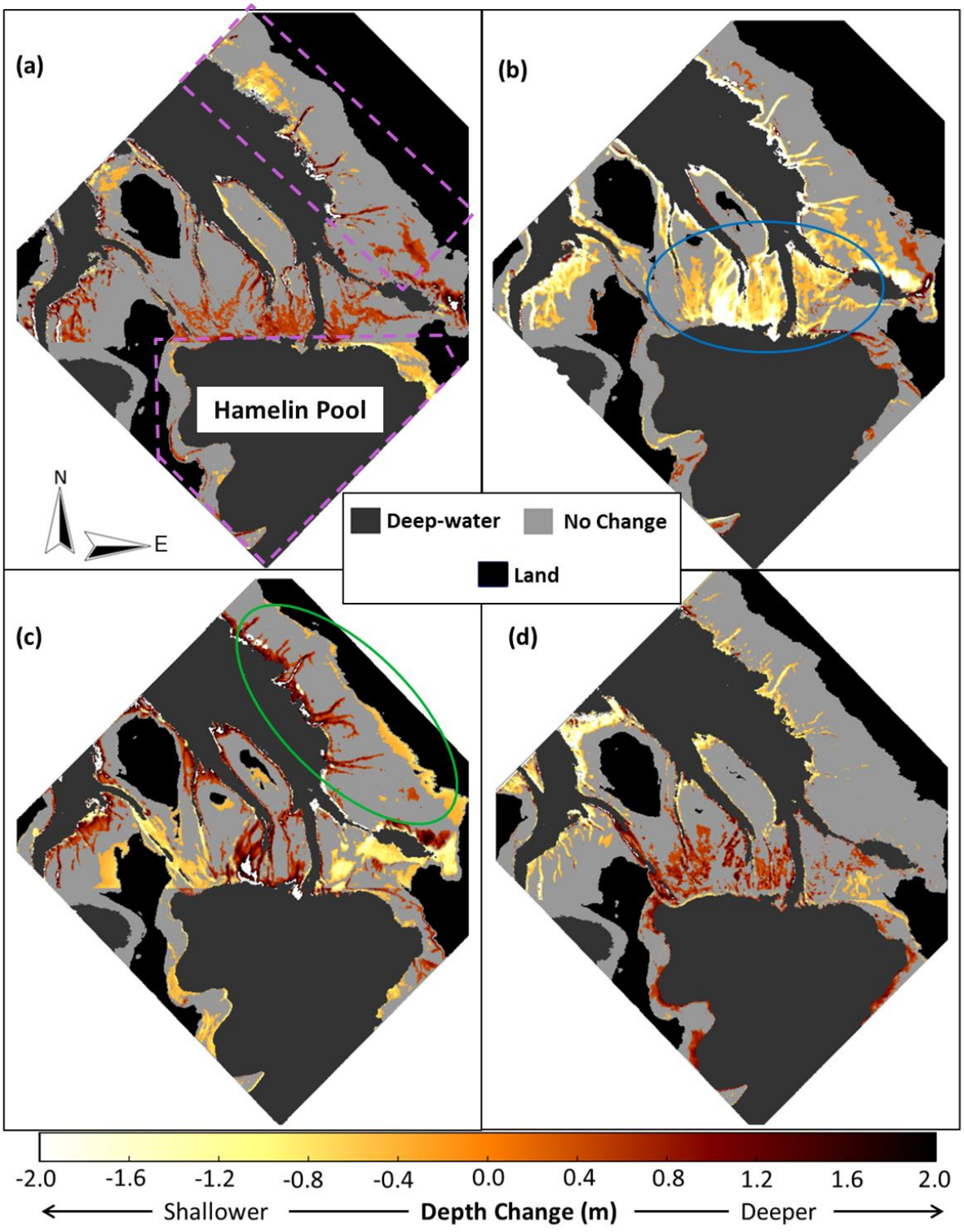

Figure 13: Change detection analysis of HICO-derived, tide corrected bathymetry of the Faure Sill between the dates of: (a) 14-Dec-2011 and 21-Jan-2012; (b) 21-Jan- and 27-Feb-2012; (c) 27-Feb- and 04-Jun-2012 and; (d) 04-Jun- and 08-Aug-2012. Deep-water and land are presented as dark and black pixels respectively. The blue and green circles in (b) and (c) highlight regions of change discussed in the text. Separate image-based tide corrections were performed for the dashed magenta presented in (a).

The HICO-derived bathymetry dataset spans both summer and winter and thus it is likely that the Faure Sill, Hamelin Pool and the Wooramel bank have substantially different tide heights. The normalization to a reference depth over the Faure Sill can therefore introduce large artificial depth changes at the other regions, and as such, separate image-based tide corrections were performed. It should be noted that separate regional tide correction and subsequent merging to a single bathymetric image can only be used to analyze temporal changes; as these images would contain steps in the depth between adjacent tide corrected regions. Tidal modeling would be necessary to interpolate (either linearly or non-linearly) the tide correction offsets for the different regions to generate a homogeneous tide corrected bathymetry image. However this is beyond the scope of this study.

The change detection analysis (Figure 13) indicates constant bathymetry for the majority of the Faure Sill. Thought there are three regions that experience bathymetric fluctuations between the five successive dates. These regions are predominantly shallow water areas: (i) on the western and eastern sides of Hamelin Pool; (ii) on the southern Faure Sill (see blue circle in figure 13b), and; (iii) on the Wooramel bank (green circle in figure 13c).

The extent of change observed ranged between approximately -1.6 m (shallower) and 1.6 m (deeper); this appears to be an unrealistic depth change in the timeframe of one month. For example on the western shallow regions of Hamelin Pool, the depth decreased by approximately 1 m from 27 February to 4 June 2012. This is unlikely to occur as the benthos of this region consists of hard microbial pavement that is not susceptible to erosion from water movement (Jahnert and Collins, 2011). Although the deposition of motile sediment and its subsequent removal is possible, the extent of change observed through the HICO-derived bathymetry is unlikely. However, we are encouraged by the spatial consistency of several features in this region, whose depth fluctuates through time.

The change in depth detected on the southern Faure Sill between 21 January and 27 February 2012 (blue circle in Figure 13b) and 27 February and 4 June 2012 (Figure 13c) appears to be due to a plume of turbid water at this location on the 27 February (see red square in Figure 14). The true color imagery on 27 February does indicate the formation of new water channels; however the change detection (Figure 13) shows that the bathymetry at this date is approximately 1 m shallower than on 21 January – contrary to the formation of new water channels. Additionally, R_{rs} spectra of this region indicate higher absorption between 400 to 500 nm than the adjacent areas, suggestive of higher CDM/phytoplankton. The retrieved model parameters over the plume on 27 February 2012 are: $a_{\phi}(440) = 0.11\ m^{-1}$, $a_{dg}(440) = 0.18\ m^{-1}$, $b_{bp}(550) = 0.12\ m^{-1}$, depth = 0.50 m, $B_{sand} = 0.115$, and $B_{seagrass} = 0.005$. The same region on the 21 January 2012 had lower IOP values, larger depth and a brighter substrate: $a_{\phi}(440) = 0.035\ m^{-1}$, $a_{dg}(440) = 0.07\ m^{-1}$, $b_{bp}(550) = 0.035\ m^{-1}$, depth = 3.5 m, $B_{sand} = 0.45$, and $B_{seagrass} = 0.02$. Given the high IOPs, very shallow depth and low bottom albedo coefficients implies that the bottom contribution to R_{rs} is very low or non-existent over this plume, and as such the retrieved depth is unreliable. In operational satellite processing, such pixels should be flagged as deep-water pixels and not used in the change detection analysis.

The shallow water region with water channels orientated perpendicular (green circle in figure 13) appears to have undergone changes in depth due to resuspension and movement of sediment near the mouth of the Wooramel River. This was observed on the 14 December 2011, where the sediment plume appeared to enter the numerous channels and flow northward (figure 14). It is possible that some sediment would have settled down, given that modeled tidal flow (Burling, 1998) is perpendicular to the channels' orientation (i.e. trapping sediment) with a modeled speed of approximately 0.5 m/s at high and low tide (Burling, 1998). Retrieved $b_{bp}(550)$ imagery on 21 January 2012 revealed that the amount of suspended sediment in the water column was considerably less, and where the change detection analysis

showed an increase in depth by approximately 1.2 m (Figure 13a). In other words, on the 14 December the water channels were 1.2 m shallower, presumably due to the high sediment deposition that was subsequently eroded over 38 days until 21 January 2012. Note the fluctuating depth changes (shallower, then deeper) for these channels are observed in figures 13b and 13c, due to more resuspension and movement of sediment from the mouth of the Wooramel River on 27 February 2012.

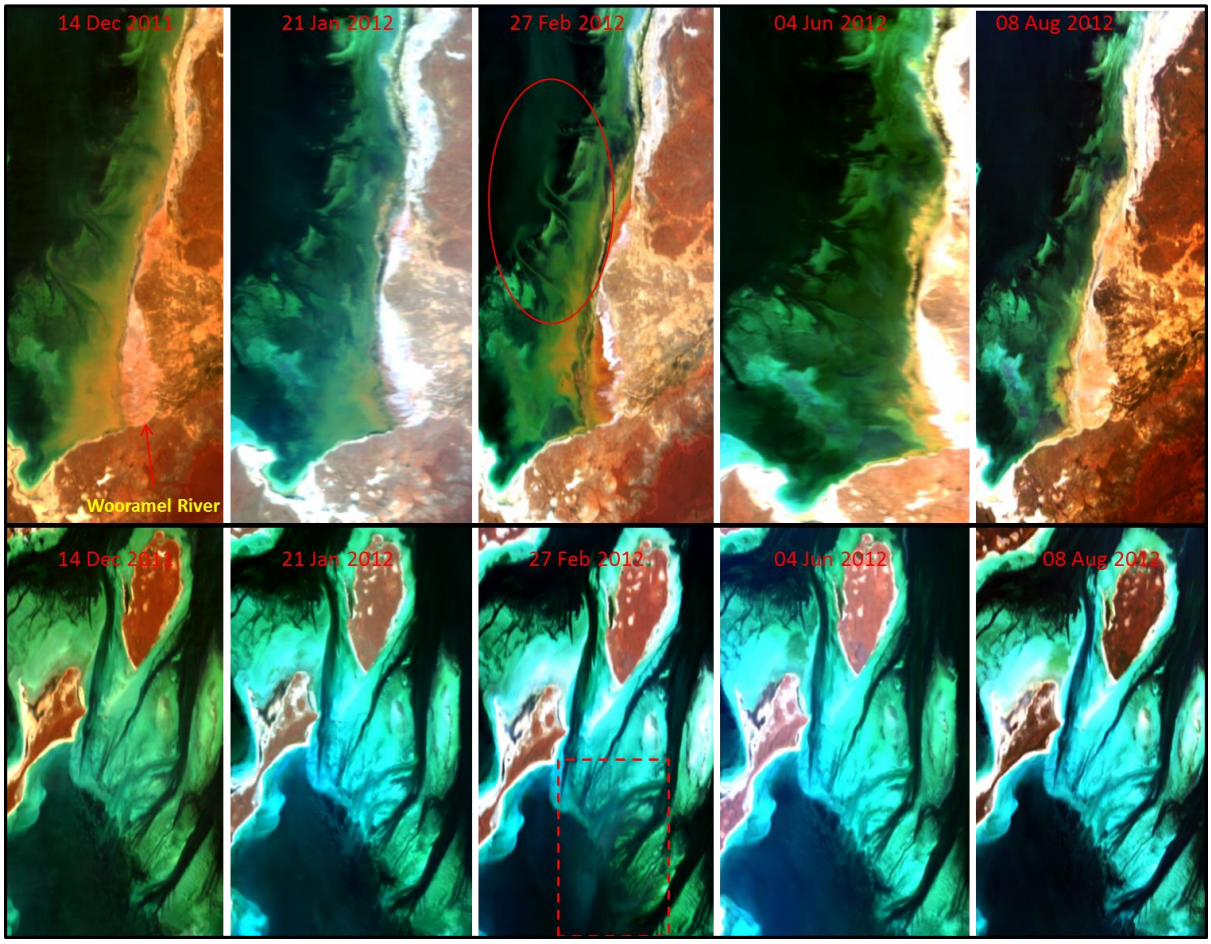

Figure 14: HICO derived pseudo true color images of: the shallow water region parallel to the coast, north of the Wooramel River (top panels), and; the Faure Sill (bottom panels). The top panels show sediment flowing north from the Wooramel River, and through the seagrass channels orientated perpendicular to the coast, indicated by the red circle. The red square on 27-Feb-2012 highlights a plume of turbid water on the southern Faure Sill (bottom panel).

The change detection analysis highlights that though some of the changes observed are feasible, the extent of change (approximately 1 m) is unlikely. The magnitude of detected change depends on the accuracy and precision of the depth retrievals and on the tide correction scheme. Firstly a relatively high precision is needed to detect change above the uncertainty. Here the low relative uncertainty in the retrieved depths of shallow water pixels (< 10%, see Figure 6) allowed the detection of subtle changes to as low as 40 cm (see Figure 13). Secondly, high accuracy in the retrieved depth (prior to tide correction) is required to infer accurate magnitudes of change. This in turn necessitates adequate atmospheric correction and a robust optimization scheme that converges to the global minimum. Here, the sub-optimal radiometric corrections have likely reduced the accuracy, particularly over the quasi-deep water pixels, whilst the convergence to local minima is the likely cause of the inaccuracy in some shallow water pixels. Future improvements to atmospheric and sun-glint corrections and optimization schemes will increase the accuracy in change detection analysis, however, this study has shown that even with sub-optimal corrections, it is possible to detect change above the uncertainty in the retrievals due to environmental and sensor noise.

4.0 Conclusion

The accuracy and precision of the HICO-derived bathymetry dataset was dependent on the quality of the atmospheric/sun-glint correction and on the BRUCE shallow water semi-analytical inversion scheme respectively. For many atmospheric correction algorithms, such as Tafkaa (Gao et al., 2000), the lack of spectral bands past 900 nm inhibits the selection of the appropriate atmospheric aerosol model and an estimation of vertical column water vapor in a per-pixel basis. To overcome this information gap, coincident MODIS level-2 products of the Shark Bay region were processed and used to obtain several of the input parameters that Tafkaa-6S required. This study has shown that the procedure introduced three

spectral artifacts to the remote sensing reflectance spectra. Unfortunately, the high absorption of light in the water column throughout Shark Bay causes the magnitude of the water-leaving reflectance to become comparable to that of the spectral artifacts – particularly over quasi-deep and optically deep water pixels. This potentially leads to inaccurate depth retrievals over these pixels. Conversely, the accuracy of the depth retrievals for shallow water were shown to be not greatly affected as the magnitude of R_{rs} for these pixels were substantially higher relative to the spectral artifacts.

Addition of spectral artifacts enhanced the complexity of the parameter space with the addition of more local minima. To increase the likelihood of the L-M algorithm localizing to a global minimum, a brief search of parameter space was performed to locate the parameter values that corresponds to a local minimum with the lowest Euclidean distance. These parameter values were then passed as the initial values to the uncertainty inversion scheme proposed by Hedley et al. (2010). This per-pixel parameter space 'update-repeat' search and uncertainty determination afforded improved retrievals of bathymetry, where the majority of the bathymetry image had a relative uncertainty of less than 20%. A per-pixel *t*-test analysis between bathymetry images at consecutive timestamps revealed the ability to detect changes in HICO-derived depth to as low as 0.4 m. This reinforces the use of satellite-based hyperspectral remote sensing techniques in analyzing time series datasets when uncertainty is taken into account.

HICO's ability to detect temporal change is not only dependent on precision of the bathymetric dataset but also on its geolocation accuracy. Thorough geo-registration using ground control points taken from Google Earth™ imagery has increased the relative geolocation accuracy, from more than 30 km using the distributed geographic lookup tables, to better than 300 m (i.e. 3 pixels). However, despite this improvement, analyzing temporal change from remotely sensed imagery requires sub-pixel geolocation accuracy, that is, less

than 100 m for HICO. Thus enabling time series analysis of HICO data requires further work in either creating automated geo-registration algorithms.

Relating changes in bathymetry to factors such as sedimentation/erosion necessitates the removal of the tidal contribution to the retrieved water column depth. Correcting tide height over the Faure Sill has proved problematic. An empirical tide correction scheme is presented that corrects each bathymetry image in the time series to a reference depth. This reference depth is arbitrary and in this case was set to the median depth across the time series. However, this reference depth can be set to a datum such as lowest astronomical tide or mean water height if these values are known for the region. Even so, with this image based normalization of depth, it was shown that detecting changes in depth due to sedimentation/deposition of as low as 0.4 m is possible. The fluctuating changes in depth (increasing then decreasing) of several spatially consistent features are particularly encouraging. Though the extent of change is at present over-estimated, improvements to atmospheric/sun-glint/air-to-water interface corrections would directly enhance the accuracy of the depth retrievals and hence extent of change.

The issues faced here in regards to atmospheric and sun-glint corrections are by no means inherent to HICO, but to all ocean color sensors. Though HICO was built as a prototype low cost sensor, its data can be manipulated to retrieve precise bathymetry. The development of future sensors that have: (1) higher SNR and SWIR bands in combination with more advanced atmospheric/sunglint correction and in water inversion algorithms could substantially improve bathymetry retrievals, and; (2) sophisticated geo-location and – registration algorithms to afford sub-pixel geolocation accuracies will also lead to the ability in monitoring changes in the bathymetry of key coastal regions.

Acknowledgements

R. Garcia would like to thank Dr. John Hedley for his assistance with the uncertainty inversion scheme and the Western Australian Department of Transport for the Carnarvon tide height data. An Australian Postgraduate Award administered through Curtin University was used to fund this research. The authors also wish to thank the HICO project team at both OSU and NRL for targeting, processing and distribution of HICO L1B data over Shark Bay. All HICO^{TM} data were provided by the Naval Research Laboratory through the Oregon State University, College of Earth, Ocean, and Atmospheric Sciences' HICO website (hico.coas.oregonstate.edu).

5.0 References

Ahmad, Z., Franz, B. A., McClain, C. R., Kwiatkowska, E. J., Werdell, J., Shettle, E. P., & Holben, B. N. (2010). New aerosol models for the retrieval of aerosol optical thickness and normalized water-leaving radiances from the SeaWiFS and MODIS sensors over coastal regions and Open Oceans. *Applied Optics*, 49(29), 5545-5560.

Bailey, S. W., Franz, B. A., & Werdell, P. J. (2010). Estimation of near-infrared water-leaving reflectance for satellite ocean color data processing. *Optics Express*, 18(7), 7521-7527.

Bicheron, P., Amberg, V., Bourg, L., Petit, D., Huc, M., Miras, B., Brockmann, C., Hagolle, O., Delwart, S., Ranera, F., Leroy, M., & Arino, O. (2011). Geolocation assessment of MERIS GlobCover orthorectified products. *IEEE Transactions on Geoscience and Remote Sensing*, 49(8), 2972-2982.

Brando V.E. Anstee J.M., Wettle M., Dekker A.G., Phinn S.R., & Roelfsema C. (2009). A physics based retrieval and quality assessment of bathymetry from suboptimal hyperspectral data. *Remote Sensing of Environment*. 113, 755-770

Burling, M. C. (1998). Oceanographic aspects of Shark Bay Western Australia. M. S. thesis, Centre Water Research, University of Western Australia, Perth, Western Australia, Australia.

Burling, M. C., Pattriaratchi, C. B., & Ivey, G. N. (2003). The tidal regime of Shark Bay, Western Australia. *Estuarine, Coastal and Shelf Science*. 57, 725-735.

Burne, R. V., & Johnson, K. (2012). Sea-level variation and the zonation of microbialites in Hamelin Pool, Shark Bay, Western Australia. *Marine and Freshwater Research*, 64, 994-1004.

Clark, R.K., Fay, T.H., & Walker, C.L. (1987). Bathymetry calculations with Landsat 4 TM imagery under a generalised ratio assumption. *Applied Optics*. 26(19), 4036-4038.

Cooper, K., S. Boyd, J. Eggleton, D. Limpenny, H. Rees, and K. Vanstaan (2007), Recovery of the seabed following marine aggregate dredging on the Hastings Shingle Bank off the southeast coast of England. *Estuarine, Coastal and Shelf Science*, 75, 547-558.

Coppin, P., Jonckheere I., Nackaerts K., & Muys B. (2004). Digital change detection methods in ecosystem monitoring: a review. *International Jorunal of Remote Sensing*, 25(9), 1565-1595.

Dai, X., & Khorram, S. (1998). The effects of image misregistration on the accuracy of remotely sensed change detection. *IEEE Transactions on Geoscience and Remote Sensing*. 36(5), 1566-1577.

Defoin-Platel, M., & Chami, M. (2007). How ambiguous is the inverse problem of ocean color in coastal waters. *Journal of Geophysical Research*, 112(C3), C03004

Dekker, A.G., Phinn, S.R., Anstee, J., Bissett, P., Brando, V.E., Casey, B., Fearns, P., Hedley, J., Klonowski, W., Lee, Z.P., Lynch, M., Lyons, M., Mobley, C., & Roelfsema, C. (2011). Intercomparison of shallow water bathymetry, hydro-optics, and benthos mapping techniques in Australian and Caribbean coastal environments. *Limnology and Oceanography, methods*. 9, 396-425.

Department of Environment and Conservation, n.d. *Birridas*. http://www.sharkbay.org/assets/documents/fact%20sheets/birridas%20v2.pdf (accessed February 4, 2013).

Dierssen, H.M., Zimmerman, R.C., Leathers, R.A., Downes, T.V., & Davis, C.O. (2003). Ocean color remote sensing of seagrass and bathymetry in the Bahamas Banks by High-Resolution airborne imagery. *Limnology and Oceanography*. 48(1 part 2), 444-455.

Doodson, A. T., & Warburg, H. D. (1941). *Admiralty Manual of Tides*, Hydrographic Department, Admiralty, London.

Egbert, G. D., & Erofeeva, S. Y. (2002). Efficient inverse modeling of barotropic ocean tides. *Journal of Atmospheric and Oceanic Technology*, 19(2), 183-204.

Fabbri, K. P. (1998). A methodology for supporting decision making in integrated coastal zone management. *Ocean and Coastal Management*. 39(1-2), 51-62.

Galparsoro, I., Borja, A., Legorburu, I., Hernandez, C., Chust, G., Liria, P., & Uriarte, A. (2010). Morphological characteristics of the Basque continental shelf (Bay of Biscay, northern Spain); their implications for Integrated Coastal Zone Management. *Geomorphology*, 118(3-4), 314:329.

Gao, B., Montes, M. J., Ahmad, Z., & Davis, C. O. (2000). Atmospheric correction algorithm for hyperspectral remote sensing of ocean color from space. *Applied Optics*, 39(6), 887-896.

Gao, B., Li R., Lucke, R. L., Davis, C. O., Bevilacqua, R. M., Korwan, D. R., Montes, M. J., Bowles, J. H., and Corson M. R. (2012). Vicarious calibrations of HICO data acquired from the International Space Station. *Applied Optics*, 51(14), 2559 – 2567.

Goodman, J. A., Lee, Z., & Ustin, S. L. (2008). Influence of atmospheric and sea-surface corrections on retrieval of bottom depth and reflectance using a semi-analytical model: a case study in Kaneohe Bay, Hawaii. *Applied Optics*, 47, F1-F11.

Goodman, J. A., Montes, M. J., & Ustin, S. L. (2003). Applying tafkaa for atmospheric correction of AVIRIS over coral ecosystems in the Hawai'ian islands. *Proceedings of the 12th AVIRIS/HYPERION Earth Science Workshop*, pp 91-96.

Green, E.P., Mumby, P.J., Edwards, A.J., & Clark, C.D. (1996). A review of remote sensing for the assessment of tropical coastal resources. *Coastal Management*, 21(1), 1-40.

Guenther, G.C., Cunningham, A.G., LaRocque, P.E., & Reid, D.J. (2000). Meeting the accuracy challenge in airborne lidar bathymetry. 20th EARSeL Symposium Workshop on Lidar Remote Sensing of Land and Sea, *European Association of Remote Sensing Laboratories*, Dresden, Germany.

Hardie, R. C., & Boncelet. C. G. (1993). LUM filters: a class of rank-order-based filters for smoothing and sharpening. *IEEE Transacstions on Signal Processing*, 41(3), 1061-1076.

Hedley, J., Roelfsema C., & Phinn S. R. (2009). Efficient radiative transfer model inversion for remote sensing applications. *Remote Sensing of Environment*, 113, 2527-2532.

Hedley, J., Roelfsema, C., & Phinn, S. (2010). Propagating uncertainty through a shallow water mapping algorithm based on radiative transfer model inversion, Proceedings of Ocean Optics XX, Anchorage.

Hedley, J., Roelfsema, C., Koetz, B., & Phinn, S. (2012). Capability of the Sentinel 2 mission for tropical coral reef mapping and coral bleaching detection. *Remote Sensing of Environment*, 120, 145-155.

Hester, D. B., Nelson, S. A. C., Cakir, H. I., Khorram, S., & Cheshire, H. (2010). High-resolution land cover change detection based on fuzzy uncertainty analysis and change reasoning. *International Journal of Remote Sensing*, 31(2), 455-475.

Hu, C., Feng, L., Lee, Z., Davis, C. O., Mannino, A., McClain, C. R., & Franz, B. A. (2012). Dynamic range and sensitivity requirements of satellite ocean color sensors: learning from the past. *Applied Optics*, 51(25), 6045-6062.

Jahnert, R., & Collins, L. B. (2011). Significance of subtidal microbial deposits in Shark Bay, Australia. *Marine Geology*, 286, 106-111.

IOCCG (2006). Remote sensing of inherent optical properties: Fundamentals, tests of algorithms, and applications. In Z. P. Lee (eds), *Reports of the International Ocean-Colour Coordinating Group*, No. 5, IOCCG, Dartmouth, Canada.

Irish, J. L., & Lillycrop, W. J. (1999). Scanning laser mapping of the coastal zone: the SHOALS system. *ISPRS Journal of Photogrammetry and Remote Sensing*, 54, 123-129.

Jahne, B. (2005). *Digital Image Processing*, 6th edn, Springer-Verlag Berlin Heidelberg, New York.

Kay S., J. D. Hedley, & Lavender S. (2009). Sun glint correction of high and low spatial resolution images of aquatic scenes: a review of methods for visible and near-infrared wavelengths. *Remote Sensing*, 1, 697-730.

Klonowski W. K., Fearns P. R. C. S, & Lynch M. J. (2007). Retrieving key benthic cover types and bathymetry from hyperspectral imagery. *Journal of Applied Remote Sensing*, 1, 011505

Ko, S-J, & Lee, Y. H. (1991). Center weighted median filters and their applications to image enhancement. *IEEE Transactions on Circuits and Systems*, 38(9), 984-993.

Lee Z. P, Carder K. L., Mobley C. D., Steward R. G., & Patch J. S. (1998). Hyperspectral remote sensing for shallow waters. 1. A semianalytical model. *Applied Optics*, 37(27), 6329-6338.

Lee Z. P, Carder K. L., Mobley C. D., Steward R. G., & Patch J. S. (1999). Hyperspectral remote sensing for shallow waters: 2. Deriving bottom depths and water properties by optimization. *Applied Optics*, 38(18), 3831-3843.

Lee, Z. P., Casey, B., Arnone, R., Weidemann, A., Parsons, R., Montes, M. J., Gao, B-C., Goode, W., Davis, C. O., & Dye, J. (2007). Water and bottom properties of a coastal environment derived from Hyperion data measured from the EO-1 spacecraft platform. *Journal of Applied Remote Sensing*, 1, 011502.

Li, R. R., Lucke, R., Korwan, D., & Gao, B-C. (2012). A Technique For Removing Second-Order Light Effects From Hyperspectral Imaging Data. *IEEE Transactions on Geoscience and Remote Sensing*, 50(3), 824-830.

Logan, B. W., & Cebulski, D. E. (1970). Sedimentary Environments of Shark Bay, Western Australia. In *Carbonate Sedimentation and Environments, Shark Bay, Western Australia*, pp. 1-37, American Association of Petroleum Geologists, Tulsa, Oklahoma.

Lucke, R. L., Corson, M., McGlothin, N. R., Butcher, S. D., Wood, D. L., Korwan, D. R., Li, R. R., Snyder, W. A., Davis, C. O., & Chen, D. T. (2011). Hyperspectral Imager for the coastal ocean: Instrument description and first images. *Applied Optics*, 50(11), 1501-1516.

Lyard, F., Lefevre, F., Letellier, T., & Francis, O. (2006). Modeling the global ocean tides: A modern insight from FES2004. *Ocean Dynamics*, 56, 394-415, doi: 10.1007/s10236-006-0086-x.

Lyzenga, D. R. (1978). Passive remote sensing techniques for mapping water depth and bottom features. *Applied Optics*, 17(3), 379-383.

Lyzenga, D. R. (1985). Shallow water bathymetry using combined lidar and passive multispectral scanner data. *International Journal of Remote Sensing*, 6(1), 115-125.

Mied, R. P., Snow, C. M., Smith, G. B., Bachmann, C. M., Korwan, D. R., Fusina, R. A., Vermillion, M. S., & Hagen, R. A. (2013). Tidal constituents from remote sensing image sequences. *Estuarine, Coastal and Shelf Science*, 117, 159-167.

Mobley C. D., Sundman L. K., Davis C. O., Bowles J. H., Downes T. V., Leathers R. A., Montes M. J., Bissett W. P., Kohler D. D. R., Reid R. P., Louchard E. M., & Gleason A.

(2005). Interpretation of hyperspectral remote-sensing imagery by spectrum matching and look-up tables. *Applied Optics*, 44(17), 3576-3592.

Montes, M. J., Gao, B-C., & Davis, C. O. (2004). NRL atmospheric correction algorithms for oceans: Tafkaa User's Guide. Naval Research Laboratory, Washington DC.

Morton, R. A. (2002). Factors controlling storm impacts on coastal barriers and beaches - a preliminary basis for near real-time forecasting. *Journal of Coastal Research*, 18(3), 486-501.

Morton, R. A., & Sallenger, A. H. (2003). Morphological impacts of extreme storms on sandy beaches and barriers. *Journal of Coastal Research*, 19(3), 560-573.

Moses, W. J., Gitelson, A. A., Berdnikov, S., Bowles, J. H., Povazhnyi, V., Saprygin, V., Wagner, E. J., & Patterson, K.W. (2014). HICO-Based NIR–Red Models for Estimating Chlorophyll-a Concentration in Productive Coastal Waters. *IEEE Geoscience and Remote Sensing Letters*, 11(6), 1111-1115,doi: 10.1109/LGRS.2013.2287458.

Paredes, J. M., & Spero, R. E. (1983). Water depth mapping from passive remote sensing data under a generalised ratio assumption. *Applied Optics*, 22(8), 1134-1135.

Paterson, K. W., & Lamela, G. (2011). Influence of aerosol estimation on coastal water products retrieved from HICO images. *Proc. SPIE 8030, Ocean Sensing and Monitoring III*, 803005 (May 04, 2011); doi:10.1117/12.883263

Philpot, W. D. (1989). Bathymetric mapping with passive multispectral imagery. *Applied Optics*, 28(8), 1569-1578.

Philpot, W., Davis, C. O., Bissett, W. P., Mobley, C. D., Kohler, D. D. R., Lee, Z., Bowles, J., Steward, R. G., Agrawal, Y., Trowbridge, J., Gould, R. W., & Arnone, R.A. (2003). Bottom characterisation from Hyperspectral image data. *Oceanography*, 17(2), 76-85.

Polcyn, F. C., Brown, W. L., & Sattinger, I. J. (1970). The measurement of water depth by remote sensing techniques. *Report 8973-26-F*, Willow Run Laboratories, U. Michigan, Ann Arbor.

Shi, W. Z., & Ehlers, M. (1996). Determining uncertainties and their propagation in dynamic change detection based on classified remotely-sensed imagery. *International Journal of Remote Sensing*, 17(14), 2729-2741.

Stumpf, R.P., Holderied, K., & Sinclair, M. (2003). Determination of water depth with high-resolution satellite imagery over variable bottom types. *Limnology and oceanography*, 48(1, part 2), 547-556.

Townshend, J. R. G., Justice, C. O., Gurney, C., & McManus, J. (1992). The impact of misregistration on change detection. *IEEE Transactions on Geoscience and Remote Sensing*, 30, 1054-1060.

Ungar, S. G. (2003). Overview of the Earth Observing One (EO-1) Mission. *IEEE Transactions on Geoscience and Remote Sensing*, 41(6), 1149-1159.

Walker, D. I., Kendrick, G. A., & McComb, A. J. (1988). The distribution of seagrass species in Shark Bay, Western Australia, with notes on their ecology. *Aquatic Botany*, 30: 305-317.

Wettle, M., & Brando, V. E. (2006). SAMBUCA: semi-analytical model for bathymetry, un-mixing and concentration assessment. *Report 22/06*, CSIRO Land and Water, <www.clw.csiro.au/publications/science/2006/sr22-06.pdf>

Wolfe, R. E., Nishihama, M., Fleig, A. J., Kuyper, J. A., Roy, D. P., Storey, J. C., & Patt, F. S. (2002). Achieving sub-pixel geolocation accuracy in support of MODIS land science. *Remote Sensing of Environment*, 83, 31-49.